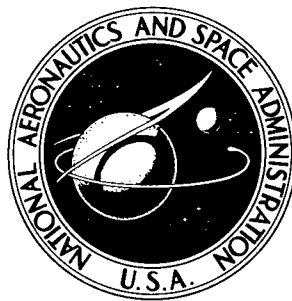


NASA TECHNICAL NOTE



NASA TN D-2836

NASA TN D-2836

O.K.

AMPTIAC

60488

DISTRIBUTION STATEMENT A

Approved for Public Release
Distribution Unlimited

ANALYSIS AND EVALUATION OF A VAPOR-CHAMBER FIN-TUBE RADIATOR FOR HIGH-POWER RANKINE CYCLES

by Henry C. Haller, Seymour Lieblein, and Bruce G. Lindow

Lewis Research Center

Cleveland, Ohio

20010720 131

ANALYSIS AND EVALUATION OF A VAPOR-CHAMBER FIN-TUBE
RADIATOR FOR HIGH-POWER RANKINE CYCLES

By Henry C. Haller, Seymour Lieblein, and Bruce G. Lindow

Lewis Research Center
Cleveland, Ohio

NATIONAL AERONAUTICS AND SPACE ADMINISTRATION

For sale by the Clearinghouse for Federal Scientific and Technical Information
Springfield, Virginia 22151 - Price \$3.00

CONTENTS

	Page
SUMMARY	1
INTRODUCTION	2
RADIATOR CONFIGURATION AND THERMODYNAMIC CYCLE.	3
HEAT-TRANSFER ANALYSIS.	5
Approach and Assumptions.	5
Radiator Fin-Tube Effectiveness.	6
Capillary Fluid Requirements	10
METHOD OF SOLUTION AND CALCULATION INPUTS	11
WEIGHT AND GEOMETRY RESULTS.	13
Radiator Weight.	13
Radiator Geometry	14
Planform area.	14
Panel aspect ratio.	15
Fin wall thickness.	15
Tube block armor thickness.	15
Number of tubes.	15
Number of fin segments.	16
COMPARISON WITH OTHER GEOMETRIES	16
Radiator Weight.	16
Radiator Geometry	17
DEGRADATION OF RADIATING EFFECTIVENESS.	18
CONCLUDING REMARKS	20
APPENDIXES	
A - SYMBOLS.	22
B - TUBE BLOCK TEMPERATURE RATIO	25
C - PRESSURE DROP	27
D - RADIATOR WEIGHT AND GEOMETRY	31
REFERENCES	38

ANALYSIS AND EVALUATION OF A VAPOR-CHAMBER FIN-TUBE RADIATOR FOR HIGH-POWER RANKINE CYCLES

by Henry C. Haller, Seymour Lieblein, and Bruce G. Lindow
Lewis Research Center

SUMMARY

An analytical investigation of a flat, direct-condensing fin-tube radiator employing segmented vapor-chamber fins as a means of improving heat rejection was performed for illustrative high-power, high-temperature Rankine space power electric generating systems. A vapor-chamber fin is obtained by replacing the conventional single solid fin with a double wall fin that forms a hollow chamber between tubes. A working fluid in the chamber can then be boiled off the tube surface and condensed on the fin surface of the chamber to produce a fin of constant temperature. Condensate is then returned to the boiling surface by some means of capillary pumping.

The analysis of the vapor-chamber fin-tube radiator considered pressure drop in the radiator tubes and headers, meteoroid protection for the tubes/headers, and vapor-chamber fins, and temperature drop in the tube armor in the development of the descriptive equations. The heat transfer, weight, and geometric characteristics of the vapor-chamber fin-tube radiator were determined over a wide range of variables for two illustrative radiator design applications.

The vapor-chamber fin-tube radiator was also compared to the more conventional solid-conducting double fin-tube and central fin-tube radiators on a weight and geometry basis for a nonredundant configuration with a high level of nonpenetration probability. It was shown that for the illustrative 500-kilowatt-cycle columbium and 1-megawatt-cycle beryllium cases chosen for the comparison of the three fin-tube geometries, the vapor-chamber fin tube is 40 to 55 percent lighter in weight than the central fin-tube radiator and from 30 to 40 percent lighter in weight than the double fin-tube configuration depending on the required thickness of the tube side wall. The vapor-chamber fin-tube radiator was also shown to have from 13 to 18 percent smaller planform (projected) area, fewer number of radiator tubes, and larger tube inner diameters than the other two fin-tube geometries at maximum heat rejection per unit weight.

Unique construction features enable the radiator to function as a solid-conducting configuration after the vapor chambers have been punctured by meteoroids; hence, the thermal effectiveness of the radiator does not decrease in direct proportion to the number of fin segments punctured.

These preliminary results warrant further investigation into the merits of employing the vapor-chamber fin-tube concept for other space radiator applications.

Lend

INTRODUCTION

A major problem in the design of large electric space powerplants using a closed power cycle such as the turbogenerator or thermionic concept is the efficient and reliable rejection of large amounts of waste heat by radiation to space. Radiators designed for the rejection of waste heat generally employ thin solid fins as an extended radiation heat-transfer surface between fluid-carrying tubes or channels. The purpose of such an arrangement is to reduce the amount of the overall radiator surface occupied by flow passages and thereby reduce the area vulnerable to critical damage from impacting meteoroids.

A radiator configuration that is frequently considered in analyses is the central fin-tube geometry, which consists of a number of parallel tubes separated by solid fins located in the plane of the tube centers (refs. 1 to 7). The fins receive heat from the fluid-carrying tubes by conduction, and heat is lost by radiation to space resulting in temperature drops along the length of the fin between adjacent tubes. As a consequence, the overall radiating effectiveness of the radiator is reduced, and the required radiator planform area and weight are increased. The minimum specific weights and corresponding planform areas achievable for a radiator system are generally the results of an optimization primarily between radiating effectiveness and meteoroid armor protection (e. g., refs. 8 and 9).

The vapor-chamber fin concept proposes to reduce radiator weight and area by providing for an essentially isothermal fin between tubes. It accomplishes this by replacing the single solid fin, which transfers heat by conduction, with a double wall fin that forms a hollow chamber, which contains a heat-transport fluid. The working fluid in the chamber can then be boiled off the tube surfaces of the chamber and condensed on the fin surfaces of the chamber to produce a fin of constant temperature and high radiating effectiveness. Condensate is then returned to the boiling surface by some means of capillary pumping that is essentially insensitive to gravity forces (ref. 10). In the radiator application, the vapor fin chamber vulnerable to meteoroid penetration can be compartmented into a large number of sealed segments to minimize the effect of puncture on the operative area. The principle of transporting heat by means of boiling and condensing a fluid in conjunction with the return of the condensate through a capillary medium has been established experimentally (refs. 10 and 11). The application of the vapor-chamber fin concept to space radiator design, however, remains to be evaluated. A form of such application will be treated in this report.

In addition to its potential effect in reducing radiator weight and surface area, the vapor-chamber fin will tend to reduce or eliminate the fin thermal stresses that normally result from the large temperature difference in the solid-conducting fin. Furthermore, even when punctured, an individual vapor-chamber compartment will not lose its entire

radiating effectiveness, since the chamber walls can still act as conventional solid-conducting fins.

This report presents an analysis of the heat transfer, weight, and geometry characteristics of a class of space radiators employing the vapor-chamber fin concept. The objective of the analysis is to determine the general characteristics of radiators employing this concept and to evaluate the relative merits of such radiators for space power system application. To effect this preliminary evaluation, numerical calculations are conducted for two illustrative examples of flat direct-condensing radiators radiating at 1700°R in a simplified Rankine electric power generating cycle. The first example is a columbium-alloy radiator for a 500-kilowatt cycle, and the second example is a beryllium radiator for a 1-megawatt cycle. Radiator heat transfer, weight, and geometry characteristics are determined for a wide range of variables such as tube inside diameter, ratio of fin length to tube block width, ratio of tube block side wall thickness to armor thickness, fin chamber boiling heat-transfer coefficient, ratio of boiling to condensing heat-transfer coefficient, fin chamber capillary mechanism weight, and fin chamber segment planform area.

Results for the vapor-chamber fin radiator are then compared to corresponding central fin and double fin radiators for the same material, cycle condition, tube and header pressure drops, and meteoroid protection criteria. In addition, the radiating effectiveness of a punctured segment of a vapor-chamber fin is approximated in order to indicate the maximum loss in effectiveness that might be encountered.

RADIATOR CONFIGURATION AND THERMODYNAMIC CYCLE

The general radiator panel configuration considered for the analysis is shown in figure 1. The configuration illustrated is a four-panel flat vapor-chamber direct-condensing radiator applicable to Rankine power cycles. Vapor from the turbine exhaust is distributed to the finned tubes by a vapor header. The heat radiated from the vapor header and fin tubes causes the vapor to condense. The condensate is then subcooled and collected in the liquid header before returning to the condensate pump.

The detailed cross section of the vapor-chamber fin-tube geometry is shown in figure 2. The geometry consists of a tube liner inserted in an armor block and two rectangular fins forming a sealed, enclosed chamber between adjacent tubes. A capillary-flow medium such as narrow grooves, woven wire mesh, or fibrous mat, lines the inner surfaces of the fin chamber and is saturated with a heat-transport fluid. The fluid used should provide a saturation pressure corresponding to the chamber operating temperature that is structurally compatible with the chamber construction. The details of the capillary medium and the mechanism of fluid transport process within the chamber is

outside the scope of this report, since the primary objective is the evaluation of a component employing an application of the concept. In order to conduct this preliminary evaluation, however, it was necessary to assume a highly simplified model for the vapor-chamber operation, with the implied assumption that satisfactory performance is realized over the range of variables considered in the analysis.

Inasmuch as the vapor chamber will lose its heat-transport action if a puncture and loss of transport fluid occur, the long fin chambers are divided into a number of sealed segments by numerous transverse bulkheads to reduce the hazard (fig. 1). The bulkhead thickness was arbitrarily taken as 0.020 inch. The planform area of each compartment A_{seg} , which determined the total number of fin segments N , was designated an independent variable. (Symbols are defined in appendix A.) The thickness of the fin t was based on the probability that a certain percentage of the segments would remain unpunctured at the end of the design lifetime of the radiator. The actual dimensions of the fin result from an optimization procedure that includes meteoroid protection considerations for the fin. The procedure of reference 12 is used with the vulnerable area assumed to be the exposed surface of the fin.

The tube liner, which is exposed to the cycle working fluid, must be capable of withstanding possible corrosion. The liner thickness must also be compatible with fabrication capabilities and structural requirements. The liner thickness was increased as the inside diameter was increased to provide necessary stiffening and strengthening of the radiator tubes. The schedule that defines the liner thickness is arbitrarily taken as $\delta_c = 0.040 D_i$ with a minimum wall thickness set at 0.020 inch.

For the vapor fin geometry of figure 2, the liner can be damaged by impacting meteoroids in two general ways. The first is by any primary impacts occurring on the outer exposed surfaces of the tube block. These impacts are assumed to obey the conventional armor penetration and damage relations developed for tubes (ref. 12) with vulnerable area given by $4R_b Z N_T$. Accordingly, the tube armor block thickness δ_a was determined by using the criterion of reference 12. The armor thickness, which is a result of the optimization procedure, is applied in full on the upper and lower surface of the tube.

A second damage source can arise from a spray of particles on the armor block side surface area $4N_T(R_o - t)Z$ resulting from impacts on the fin surfaces. In view of the bumper action involved and the obliquity of the secondary impacts, however, a reduction will undoubtedly be allowed in the armor thickness required by the tube block side wall to resist the effects of these secondary impacts. Furthermore, when a wire mesh or fibrous surface is used as the capillary medium, it is likely that additional resistance to secondary particles may be obtained.

A significant parameter δ_s/δ_a is therefore defined as the ratio of the armor thickness retained on the enclosed side of the tube block to the side not enclosed (fig. 2). Since no specific relations are available at present for the determination of this side-wall

thickness, a parametric variation of the ratio δ_s/δ_a was used to permit examination of the effects of reduced side-wall thickness on radiator weight and geometry.

The vapor header takes the form of a hollow paraboloid, which permits the assumption of constant fluid velocity, with a 0.12-inch liner, which was arbitrarily chosen, and a meteoroid protection thickness the same as that required by the tubes. The total vulnerable area chosen for the calculation of the armor thickness was comprised of twice the projected area of the tube block plus the outer surface of the vapor header. For simplicity, the liquid header was designed with a constant diameter and a fluid exit velocity of 4 feet per second, so that a very small pressure drop would result. The liner for the liquid header follows the same schedule with the inside diameter as do the tube liners. A maximum liner thickness is set at 0.12 inch. The liquid header also has meteoroid armor thickness equal to that obtained for the tubes. No heat radiation or subcooling is credited to the liquid header because of its relatively small diameter.

The fin-tube geometries used for comparison are the double fin-tube and central fin-tube configurations illustrated in figure 3. Comparable assumptions and input conditions were used for the radiators based on these two geometries with details of the analysis given in reference 9.

The thermodynamic cycle used for illustrative purposes in this analysis is a simplified Rankine cycle that uses a working fluid which undergoes a change of phase. The working fluid is condensed in the radiator, which results in near isothermal conditions prevailing in the tubes and the vapor header. In order to show sample results and compare the two fin-tube geometries over a range of conditions, two power levels were chosen. Potassium was chosen as the working fluid in the cycle for both power levels with a peak turbine inlet temperature of 2460°R and a radiator temperature of 1700°R . It was also specified that the radiator tubes would subcool the working fluid 100°R . Additional cycle requirements, such as turbine and generator efficiencies, were set at 0.75 and 0.90, respectively, with 10 percent of the generator output diverted for accessories and controls. The emittance of the radiator surface was taken to be 0.90. The foregoing values plus the cycle temperatures, working fluid, and the power level chosen for the analysis and comparison enabled the determination of the total heat rejection rate (7.86×10^6 Btu/hr at 500 kW and 1.572×10^7 Btu/hr at 1 MW), the mass flow rate of the working fluid, and the quality of the working fluid entering the vapor header. The analysis of the thermodynamic cycle used is given in detail in reference 8.

HEAT-TRANSFER ANALYSIS

Approach and Assumptions

The heat-transfer analysis of the vapor-chamber fin-tube geometry considers two heat flow paths in the cross section of figure 2. The working fluid in the tube gives up its

heat to the inner surface of the tube at temperature T^* . Part of this heat, Q_b , travels by conduction to the outer surfaces of the tube block where it is radiated at temperature T_b . The remainder of the heat Q_w is conducted to the tube block side wall at temperature T_w . This heat is then transferred to the fin surfaces by the boiling of the capillary heat-transport fluid on the block surface and condensing of the fluid on the fin surface. The condensate on the fin surfaces is returned to the block surface by capillary flow. The fin surface temperature is T_f and the chamber fluid saturation temperature is T_s .

The following specific assumptions were used in the development of the heat-transfer relations for the vapor-chamber fin-tube geometry:

- (1) The radiator outer surfaces act as grey bodies with emitted radiation governed by Lambert's cosine law.
- (2) Hemispherical radiation to space is from both outer surfaces of the radiator to a 0° R space sink temperature.
- (3) The tube block outer surface temperature and fin temperature are constant along the length of the tube.
- (4) Separate steady-state heat flow paths previously mentioned are analyzed on a one-dimensional basis in the tube block.
- (5) The boiling and condensing heat-transfer coefficients on the chamber surfaces are known and will be varied parametrically.
- (6) Steady-state heat transport occurs within the vapor chamber with uniform vapor saturation temperature.
- (7) The transverse bulkheads are adiabatic surfaces.
- (8) The temperature of the fin surface and each block surface is uniform.
- (9) Material properties such as thermal conductivity, modulus of elasticity, and emittance are constant and based on the radiator inlet temperature.
- (10) The inside tube wall temperature is uniform circumferentially and equal to the static temperature of the fluid evaluated at the inlet conditions of the tube.
- (11) Additional heat input to the fin by conduction from the tube block and by radiation from the block side-wall surface is negligible.
- (12) There is no temperature drop in the tube liner.
- (13) The tube block side-wall temperature is equal to the tube block outer-wall temperature (see appendix B).

Radiator Fin-Tube Effectiveness

Considering the cross-hatched portion of the cross section of the fin-tube geometry shown in figure 2 and employing the aforementioned assumptions result in the net radiant heat rejection from both the upper and lower fin surfaces of length ℓ given by

$$Q_f = 2\sigma\epsilon\ell T_f^4 Z \quad (1)$$

The heat is supplied to the fin by condensation of the heat-transport fluid on the inner surface of the fin and is given by the expression

$$Q_C = 2h_C\ell(T_s - T_f)Z \quad (2)$$

This energy, in turn, is equal to the amount of heat required to boil the heat-transport fluid on the tube block side wall

$$Q_B = 2h_B(R_o - t)(T_b - T_s)Z \quad (3)$$

Furthermore, since

$$Q_f = Q_C = Q_B \quad (4)$$

the temperature of the fin T_f can be expressed in terms of the tube block surface temperature T_b by the simultaneous solution of equations (1) to (3) to obtain

$$T_f + \frac{\sigma\epsilon}{h_B} \left(\frac{\ell}{R_o - t} + \frac{h_B}{h_C} \right) T_f^4 = T_b \quad (5)$$

Equation (5) can be rewritten into a dimensionless form by dividing both sides of the equation by T_b to yield

$$\frac{T_f}{T_b} + \lambda \left(\frac{T_f}{T_b} \right)^4 = 1 \quad (6a)$$

where the dimensionless fin heat-transfer parameter λ is

$$\lambda = \frac{\sigma\epsilon T_b^3}{h_B} \left(\frac{\ell}{R_o - t} + \frac{h_B}{h_C} \right) \quad (6b)$$

Solutions of equations (6), which relate the ratio of fin temperature to tube block surface temperature T_f/T_b , as a function of λ are shown plotted in figure 4. These re-

sults indicate the T_f/T_b ratio decreases as the value of λ increases. In effect, an increase in λ can be brought about by increasing fin length, decreasing the condensing heat-transfer coefficient, or decreasing the boiling heat-transfer coefficient. The curve is cut off at $T_f/T_b = 0.90$ since a temperature ratio below this value would lie beyond the limits of the assumption that no heat transfer to the fins exists by conduction and net internal fin chamber radiation.

In order to obtain the fin temperature T_f as a function of the tube inner-wall temperature T^* , an additional relation is required that relates the tube block wall temperature T_b to T^* . The inside tube wall temperature T^* , taken equal to the static (saturation) temperature of the working fluid vapor at the tube inlet, is determined from the expression

$$T^* = T_3 \left(1 - \frac{1}{2} \frac{K_H u_0^2}{Jgh} \right) \quad (7)$$

where T_3 is the radiator fluid stagnation temperature at the header inlet (obtained from cycle calculations, ref. 8) in degrees Rankine, K_H is the fluid turning pressure loss factor (taken as 1.15), and u_0 is the tube inlet vapor velocity.

The heat transmission by conduction to the side surface of the block is assumed to go a length δ_s over a cross-sectional area $2(R_o - t)Z$. This expression is, with $T_w = T_b$,

$$Q_w = \frac{2k(R_o - t)}{\delta_a \frac{\delta_s}{\delta_a}} (T^* - T_b)Z \quad (8)$$

Equating equations (1) and (8), under the condition that the heat rejection rates of equations (1) to (3), and (8) are equal, that is,

$$Q_f = Q_C = Q_B = Q_w$$

yields the fin temperature T_f in terms of T^* and T_b , which is given by the expression

$$T_f^4 = \frac{k(R_o - t)}{\delta_a \sigma \epsilon \ell \frac{\delta_s}{\delta_a}} (T^* - T_b) \quad (9)$$

Thus, the simultaneous solution of equations (5) and (9) yield the fin temperature T_f and the tube block surface temperature T_b as a function of T^* , which enable the formation of the ratio T_f/T_b . This ratio is plotted as a function of the boiling heat-transfer coefficient h_B for an illustrative 500-kilowatt and a 1-megawatt system in figure 5. These curves are dependent on the ratio h_B/h_C and the tube block side-wall thickness ratio δ_s/δ_a . For equal boiling and condensing coefficients, it is seen that fairly low values of h (order of 700 Btu/(hr)(sq ft)($^{\circ}$ F), which are easily attained) can be used to maintain the fin-base temperature ratio above 0.96. If $h_B/h_C = 10$, however, a boiling coefficient of at least 2000 must be achieved to maintain the same ratio of T_f/T_b .

After the temperature of the fin has been determined, the net heat transferred by both sides of a fin chamber of length ℓ can be calculated by using equation (1). This equation can be placed in dimensionless form by comparing the actual heat rejection to the total heat loss from both sides of an isothermal fin chamber of length ℓ radiating at the tube block temperature T_b . This expression, defined as the thermal efficiency of the fin, is given by

$$\eta_f = \frac{Q_f}{2\sigma\epsilon\ell T_b^4 Z} = \left(\frac{T_f}{T_b}\right)^4 \quad (10)$$

The fin thermal efficiency, as expected, is a function only of the ratio of fin to base temperature given by equations (5) and (9).

The net heat loss from the tube block surface is the emission from the outer surface, since there is no incident energy from other parts of the system or a space sink temperature. Considering both sides of the block surface of length R_b , the heat loss can be written

$$Q_b = 2\sigma\epsilon R_b T_b^4 Z \quad (11)$$

so in terms of the base surface temperature the block surface efficiency is unity.

The total radiating effectiveness based on base surface temperature is defined for the vapor fin configuration as

$$\eta_R^* = \frac{Q_f + Q_b}{2\sigma\epsilon\ell Z \left(1 + \frac{R_b}{\ell}\right) T_b^4} = \frac{\left(\frac{T_f}{T_b}\right)^4 + \frac{R_b}{\ell}}{1 + \frac{R_b}{\ell}} \quad (12)$$

The total radiating effectiveness is thus simply a function of the fin to block temperature ratio and length ratio. The fin profile ratio R_b/ℓ in equation (12) is given in terms of the tube block side-wall ratio by the expression

$$\frac{R_b}{\ell} = \frac{R_o - \left(1 - \frac{\delta_s}{\delta_a}\right)\delta_a}{L + \left(1 - \frac{\delta_s}{\delta_a}\right)\delta_a} \quad (13)$$

Using the results of equation (6a) for obtaining the fin temperature ratio along with equation (12) yields the total vapor-chamber fin-tube effectiveness η_R^* as a function of the heat-transfer parameter λ and the ratio ℓ/R_b . Figure 6 shows plots of η_R^* against λ for several values of ℓ/R_b in the range of fin temperature to tube block surface temperature ratios within the limits of the assumptions used in the analysis. The curves of figure 6 show decreasing total effectiveness with increasing λ and ℓ/R_b .

Capillary Fluid Requirements

The capillary fluid flow requirements for the vapor chamber are determined by the heat flux at the boiling surface and the latent heat of vaporization of the capillary fluid chosen. The boiling heat flux is determined by means of equation (8), which determines the heat conducted through the side wall. Taking equation (8) and dividing both sides of the equation by the cross-sectional area $2Z(R_o - t)$ yield

$$\frac{Q_w}{A} = \frac{k}{\delta_a \frac{\delta_s}{\delta_a}} (T^* - T_b) \quad (14)$$

The boiling heat flux obtained from solutions of equation (14) with inputs obtained from the results of the radiator optimization is plotted in figure 7 for the radiators associated with the 500-kilowatt (columbium) and 1-megawatt (beryllium) systems for the required range of the program inputs. The required heat flux is of the order of 2×10^4 Btu per hour per square foot in both cases, with a tendency for the flux to increase somewhat with increasing tube inner diameter. A test of a capillary wick with sodium at approximately 2000°R has produced a limiting heat flux of 9.5×10^4 Btu per hour per square foot after which local overheating occurred (ref. 10). Other tests using water as the capillary

fluid (ref. 13) have yielded a heat flux range between 1000 to 10 000 Btu per hour per square foot.

The mass flow rate of the capillary fluid is determined by setting equation (8) and the following expression equal to each other:

$$Q_B = \dot{m}hZ \quad (15)$$

where \dot{m} is the mass flow rate per unit length of radiator tube and h is the latent heat of vaporization. The resultant expression is

$$\dot{m} = \frac{2k(R_o - t)}{\delta_a \frac{\delta_s}{\delta_a} h} (T^* - T_b) \quad (16)$$

In equation (16) it is assumed that heat is added equally to the capillary fluid over the entire boiling surface.

Results for equation (16) are plotted in figure 8 for both power levels and three choices of capillary fluid. Lithium, which has the highest latent heat, had the lowest mass flow rate of the three fluids. The mass flow rates also increased with increasing inside tube diameter because of the aforementioned increase in boiling heat flux with diameter. The vapor pressures of the three fluids selected corresponding to boiling and condensing heat-transfer coefficients of 1×10^3 Btu per hour per square foot per $^\circ\text{F}$ (which results in a boiling surface temperature of 1600°R) are approximately 3.0, 0.58, and 1.25×10^{-3} pounds per square inch absolute for potassium, sodium, and lithium, respectively. The capillary material system selected will have to be capable of continuously supplying these indicated flow rates in order to achieve a steady-state operation. Tests of a heat pipe with sodium in wire screen wicks indicate that the flow rates calculated for sodium in figure 8 are achievable (ref. 11).

METHOD OF SOLUTION AND CALCULATION INPUTS

The calculation of vapor-chamber fin-tube radiator weight and geometry requires consideration not only of the heat-transfer relations described previously but also the pressure drop and meteoroid protection requirements. Detailed equations describing the tube and header pressure drop are given in appendix C, and the radiator weight and geometry relations along with meteoroid protection considerations are given in appendix D. Radiator solutions using the results of the analysis were obtained from an iterative pro-

cedure programed into an electronic digital computer. The general approach and procedure used were the same as that in reference 8.

Program inputs required were tube internal diameter, radiator vapor inlet temperature, cycle power level and conditions, properties of materials of construction and cycle fluid, meteoroid protection criterion, vapor-chamber boiling and condensing heat-transfer coefficients, vapor-chamber segment planform area, capillary material weight, tube block side-wall thickness ratio, pressure drop in the tubes and header, and chamber bulkhead thickness. Simultaneous solution of equations (5), (7), (9), (12), (B8), (C7), (C9), (D2), (D8), (D15), and (D16) result in values of the parameters δ_a , T_b , X_{VH} , N_T , and u_0 . From these are obtained the tube length Z , tube outside radius R_o , number of fin segments N , fin thickness t , panel width w , and the inside diameter of the vapor header. These latter terms, in conjunction with N_T , are then used to determine radiator weight and geometry.

The first case considered is a 500-kilowatt system with the radiator at 1700°R . For this case, the tube armor, tube liner, and the fin were all taken to be columbium - 1-percent zirconium alloy. The second case considered is a 1-megawatt electrical output powerplant with the radiator at 1700°R . The tube armor and the fin were made of beryllium, and the tube liner was of the same columbium alloy. Although there exists doubt as to the practicality of using beryllium fins when in contact with an alkali-metal capillary fluid, the material was used to represent the most optimistic situation with respect to material selection. For simplicity, the capillary and bulkhead material was assumed the same as the fin material. Both radiator cases considered the fluid stagnation temperature to be 1700°R at the header inlet. Tube inside diameters of $\frac{1}{2}$, $\frac{3}{4}$, 1, and $1\frac{1}{4}$ inch were chosen with tube lengths increased to allow 100° of subcooling. A 500-day mission time and nonpenetration probability $P(0)$ of 0.995 were chosen for the calculation of the tube and header meteoroid protection thickness in order to represent a very severe reliability requirement with a nonredundant configuration. A nonpenetration probability of 0.90 was specified for the segmented vapor-chamber fins along with the assumption that 25 percent of the fin segments would be punctured at the end of the mission. Pressure drop ratios for the two cases were set at $\Delta P/P = 0.02$ for the vapor header and $\Delta P/P = 0.05$ for the radiator tubes. Three values of the tube side-wall thickness to tube armor thickness ratio were used ($\delta_s/\delta_a = 0, 0.5, \text{ and } 1.0$) along with fin segment planform areas of 10, 20, and 40 square inches. Vapor-chamber boiling heat-transfer coefficients and the ratio of the boiling to condensing heat-transfer coefficients were also parametrically varied, and two values of vapor-chamber capillary weight material were assumed for each of the power levels investigated. The emittance of the surface coating on the fins, tubes, and headers was taken to be 0.90.

Radiator material properties were assumed constant with temperature and evaluated at 1650°R . The all-columbium alloy radiator used a material density of 530 pounds

mass per cubic foot, a thermal conductivity of 34 Btu per hour per foot per $^{\circ}\text{R}$, and a modulus of elasticity of 0.202×10^{10} pounds force per square foot. The beryllium radiator used a density of 115 pounds mass per cubic foot, a thermal conductivity of 51.5 Btu per hour per foot per $^{\circ}\text{R}$, and a modulus of elasticity of 0.397×10^{10} pounds force per square foot. The beryllium radiator used a columbium liner with the material properties previously mentioned.

Calculation procedures using pertinent inputs and specifications for the double fin-tube geometry are given in reference 9, and for the central fin-tube geometry are given in reference 8. All three radiator configuration calculations used the same inputs of material constants, thermodynamic cycle inputs, meteoroid protection criteria, pressure drops in the tubes and headers, and cycle fluid properties.

WEIGHT AND GEOMETRY RESULTS

Radiator Weight

The heat rejection per unit weight Q_{rej}/W for the vapor-chamber fin radiator was plotted for each value of tube inside diameter D_i , tube side-wall ratio δ_s/δ_a , boiling heat-transfer coefficient h_B , ratio of boiling to condensing heat-transfer coefficients h_B/h_C , fin segment planform area A_{seg} , and capillary material weight $\rho_w \delta_w$ chosen for the comparison over a range of the parameter ℓ/R_b . Results showing the variation in heat rejection rate per unit weight as a function of the ratio ℓ/R_b for three values of tube block side-wall thickness ratio and two values of the boiling heat-transfer coefficient are plotted for a given tube inner diameter for the two sample cases in figure 9. Each curve at constant h_B is seen to peak at a specific value of ℓ/R_b unless a cutoff occurs due to an imposed limitation on the vapor velocity at the inlet to the radiator tubes. This limiting velocity was set at 1300 feet per second and corresponded to a Mach number of 0.71 at the tube inlet. As seen in the figure, peak values of Q_{rej}/W are characterized by relatively high values of tube inlet vapor velocity. The double and central fin-tube radiators reached peak Q_{rej}/W at inlet velocities between 900 to 1000 feet per second.

The value of Q_{rej}/W increases as the boiling heat-transfer coefficient increases since large values of h_B and h_C allow a higher average fin temperature. The value of ℓ/R_b at peak Q_{rej}/W is seen to decrease slightly as the value of h_B is increased. The pronounced effect of a reduction in tube block side-wall thickness in increasing the value of Q_{rej}/W is clearly indicated in figure 9. The substantially greater heat rejection to weight ratio of the beryllium radiator (at a higher power level) compared to the columbium radiator is also seen.

Values of the maxima for each constant h_B curve for the three values of δ_s/δ_a of figure 9 along with results for additional tube inside diameters are shown plotted in figure 10 as a function of tube inside diameter. The increase in peak Q_{rej}/W resulting from higher values of condensing and boiling coefficients is a direct reflection of the increase in fin surface temperature (and therefore radiating effectiveness) resulting from these coefficient values (fig. 6). According to figure 10, the maximum Q_{rej}/W occurs at a smaller value of tube inside diameter as the tube side-wall thickness ratio δ_s/δ_a is decreased. However, a sizable variation in the choice of tube inside diameter can be afforded with little reduction in the value of Q_{rej}/W because of the essentially flat nature of the curves near the peak values.

In figure 11, the ratio ℓ/R_b for peak Q_{rej}/W is plotted against tube inside diameter for the vapor-chamber fin-tube geometry. The curves, which are given for both power levels and three values of δ_s/δ_a , indicate only a small variation in ℓ/R_b at peak Q_{rej}/W over the range of tube diameters from $\frac{1}{2}$ to $1\frac{1}{4}$ inches. Increasing the value of δ_s/δ_a decreases the ratio ℓ/R_b with the 500-kilowatt radiator having the largest value of ℓ/R_b at any choice of δ_s/δ_a .

Only a small reduction in maximum Q_{rej}/W occurs when the value of the fin segment planform area is increased in order to reduce the number of segments involved, as shown in figure 12. The decrease in maximum Q_{rej}/W with A_{seg} is most pronounced for $\delta_s/\delta_a = 0$ since the fin constitutes a relatively greater ratio of the total weight. For the 500-kilowatt case, a 6 percent reduction on maximum Q_{rej}/W occurs when the fin segment planform area is increased from 10 to 40 square inches at $\delta_s/\delta_a = 0.5$. A corresponding 3 percent reduction occurs for the 1-megawatt case at $\delta_s/\delta_a = 0.5$. An increase in segment area from 10 to 40 square inches corresponds, for example, to an increase in axial spacing from 2 to 8 inches for a typical fin total length of 5 inches. These reductions in Q_{rej}/W are brought about because the individual fin segment penetration probability increases as the fin segment area increases, which results in an increased fin chamber wall thickness and resultant fin weight. Large values of A_{seg} might also involve structural problems. The fin segment planform area might be dictated by radiator fabrication considerations since the number of segments greatly increases as the value of A_{seg} decreases.

The effect of varying the fin chamber capillary material weight on the radiator heat rejection per unit weight is shown in figure 13. Increasing the value of the parameter $\rho_w \delta_w$ results in a decrease in the value of Q_{rej}/W . Once again, the largest variation occurred when δ_s/δ_a equals zero, because at this condition the ratio of fin weight to overall weight is greatest.

Radiator Geometry

Planform area. - The planform area of the vapor-chamber fin-tube geometry at peak

Q_{rej}/W is shown plotted against tube diameter in figure 14 for several values of δ_s/δ_a and h_B . In both cases, increasing the heat-transfer coefficient and reducing the tube side-wall thickness ratio for peak Q_{rej}/W result in a reduction in planform area over the entire range of tube inside diameters investigated. The radiator planform area is increased, however, as the tube inside diameter is increased.

Panel aspect ratio. - Radiator panel aspect ratio, which is defined as the ratio of panel width w to tube length Z for the four-panel radiator of figure 1 is shown plotted in figure 15 for the peak Q_{rej}/W condition for two values of h_B and $\delta_s/\delta_a = 0.5$. The aspect ratio of a panel is seen to decrease sharply as the tube inside diameter increases for all cases investigated. This sharp decrease is encountered because as the tube diameter increases, the individual tube length Z increases for a given pressure drop, thus resulting in low values of aspect ratio. A small decrease in aspect ratio with reduced δ_s/δ_a occurred but is not shown in figure 15. This was primarily a result of a reduced value of ℓ/R_p as indicated in equation (D5), which describes tube length, and equation (C3), which describes the total panel width w . In general, variation of boiling and condensing heat-transfer coefficients, fin segment area, capillary weight, and tube side-wall thickness ratio had only a small effect on the magnitude of w/Z .

Fin wall thickness. - The vapor-chamber fin wall thickness is governed primarily by meteoroid protection considerations since heat transfer by conduction along the fin is assumed to be nonexistent in the analysis. The fin thickness at peak Q_{rej}/W is plotted against fin segment planform area in figure 16. It is seen that increasing the fin segment planform area increases fin wall thickness. The increased thickness as required by probability considerations is a result of the reduction in total number of fin segments as individual segment area is increased (eq. (D13)). The varying of boiling and condensing heat-transfer coefficients, tube block side-wall thickness ratio, and capillary weight resulted in a negligible change in fin wall thickness. The magnitude of the fin wall thickness obtained for the two sample cases are reasonable and should satisfy structural and fabrication requirements.

Tube block armor thickness. - Variation of maximum tube block armor thickness at peak heat rejection per unit weight with tube inside diameter is shown plotted in figure 17. The armor thickness decreases as the δ_s/δ_a ratio decreases for both the 500-kilowatt and 1-megawatt radiators. This is caused by a reduction in the vulnerable area of the tube block (function of R_p) with decreasing δ_s/δ_a . The results for the 1-megawatt case show larger values of δ_a since a larger power level increases the vulnerable area. The values of armor thickness obtained represent a very severe protection requirement because of the assigned high nonpenetration probability (0.995) without redundancy.

Number of tubes. - The number of radiator tubes for the vapor-chamber fin-tube geometry was found to decrease substantially as the tube inside diameter increased for both examples as shown in figure 18. Both curves, which are obtained for maximum

Q_{rej}/W conditions, showed little variation with tube block side-wall thickness ratio, boiling and condensing heat-transfer coefficients, fin segment planform area, and capillary weight.

For simplicity and reliability of fabrication, it is desirable to reduce the number of tubes involved in a radiator design. The vapor-chamber fin-tube geometry allows for a sizable reduction in the number of tubes with only a small reduction in Q_{rej}/W by operation at large tube inside diameters. For the 500-kilowatt case with tube block side-wall ratio set at 0.5, a 1-inch tube inside diameter results in 40 tubes with less than a 2 percent reduction in Q_{rej}/W from the maximum value. The 1-megawatt case with δ_s/δ_a set at 0.5 required just 50 tubes at $1\frac{1}{4}$ -inch tube inside diameter with a reduction in Q_{rej}/W of only 6 percent.

Number of fin segments. - The variation in the number of vapor-chamber fin segments with fin segment planform area is shown plotted in figure 19. The number of fin segments, of course, varies inversely with the fin segment planform area. Variations in tube diameter, boiling and condensing heat-transfer coefficients, tube block side-wall ratio, resulted in only small perturbations in the number of segments. The number of fin segments is quite large, regardless of the choice of fin segment planform area considered. Although it is desirable for fabrication reasons to operate at high values of A_{seg} , increased values of A_{seg} decrease the value of maximum Q_{rej}/W (fig. 12) and thus a conflicting situation is obtained.

COMPARISON WITH OTHER GEOMETRIES

The vapor-chamber fin tube is compared to the solid-conducting central and double fin-tube radiators in this section on the basis of weight, planform area, number of tubes, fin thickness, tube armor thickness, and fin-tube L/R_o ratio.

Radiator Weight

The heat rejection per unit weight results of the vapor-chamber fin-tube configuration for two values of fin segment area are compared to the double and central fin-tube results in figure 20 for the 500-kilowatt and 1-megawatt cases. It is observed that the vapor-chamber fin-tube configuration gives a substantially greater value of maximum Q_{rej}/W than the other fin-tube geometries over the entire range of tube inside diameters investigated. Compared to the central fin-tube radiator, the vapor-chamber fin-tube radiator at $\delta_s/\delta_a = 0.5$ represents an average increase in maximum Q_{rej}/W of from around 58 to 63 percent for the 1-megawatt case and from 82 to 91 percent for the

500-kilowatt case. Compared to the double fin radiator at $\delta_s/\delta_a = 0.5$ for the 1-megawatt case increases in maximum Q_{rej}/W of from 46 to 51 percent are indicated for the vapor fin radiator. These can be increased to 61 to 69 percent for the 500-kilowatt case. If the tube block side-wall ratio δ_s/δ_a can be reduced below 0.5, even greater increase in maximum Q_{rej}/W (over 100 percent) result.

Tabulated values of relative radiator specific weight for the three configurations at maximum Q_{rej}/W based on the central fin-tube radiator are shown in table I for both power levels. These results are based on a meteoroid nonpenetration probability for the tubes and headers of $P(0) = 0.995$. A reduction in the assigned value of $P(0)$ and the use of redundant radiator segments would tend to reduce the relative differences.

Radiator Geometry

Comparison of the planform area results of the vapor-chamber fin-tube geometry with those of the double and central fin-tube geometries is shown plotted in figure 21 for the two power levels investigated. The planform area of the vapor chamber fin-tube geometry is relatively insensitive to tube inside diameter and thus allows a wide choice of tube diameter and number of tubes without compromising planform area or system weight. It is seen that a sizable decrease in radiator planform area is afforded by the vapor-chamber fin-tube geometry over the other two fin-tube configurations over the entire range of tube inside diameters investigated for both radiators. For both power levels considered, the vapor-chamber fin tube gives reductions in planform area of around 15 to 20 percent over the central fin tube over the full diameter range. Relative planform areas at maximum Q_{rej}/W are given in table II. The vapor fin affords an even greater reduction in planform area compared to the double fin-tube geometry at large tube inside diameters, especially for the 500-kilowatt case.

The number of radiator tubes for the three geometries was found to decrease substantially as the tube inside diameter increases as shown in figure 22 for the 500-kilowatt and 1-megawatt systems. In general, for both power levels, the vapor-chamber fin tube had the least number of tubes for any specific choice of tube inside diameter. Comparison of the number of tubes for the three radiators at maximum heat rejection per unit weight (obtained from fig. 20) for the 500-kilowatt case at $\delta_s/\delta_a = 0.5$ indicated the vapor-chamber fin tube required 60 tubes whereas the central fin tube had approximately 230 tubes and the double fin tube had 270 tubes. This trend also held for the 1-megawatt case for which the vapor-chamber fin tube at $\delta_s/\delta_a = 0.5$ required 100 tubes compared to 190 for the central fin tube and 340 for the double fin-tube radiator at $\delta_s/\delta_a = 0.5$.

Comparison of the total fin thickness obtained for the three fin-tube configurations is shown in figure 23 for the 500-kilowatt and 1-megawatt systems. The total fin thickness of the vapor-chamber radiator was constant with tube inner diameter, and there was negligible variation of fin thickness with δ_s/δ_a , capillary material weight, or heat-transfer coefficients. The total thickness of the fin material of the vapor-chamber fin tube was less than that obtained for the solid-conducting fin configurations for both power levels over the entire range of the tube inside diameter investigated. For the 500-kilowatt columbium case, the actual thickness of the vapor-chamber fin is 0.020 inch whereas the double fin varied between around 0.027 to 0.048 inch and the central fin from around 0.07 to 0.11 inch over the range of tube inside diameters investigated. At the 1-megawatt power level with a beryllium radiator, the vapor fin thickness again remained around 0.020 inch, but both the double fin and central fin values increased substantially.

Figure 24 shows a plot of tube armor thickness δ_a against tube inside diameter for the three geometries investigated. For both power levels it is observed that the armor thickness shows little variation with diameter. In both cases the vapor-chamber fin tube has the smallest values of δ_a because of the smaller vulnerable area, which results from the nature and high thermal effectiveness of this geometry. The central fin-tube configuration has the largest armor thickness since its vulnerable area is based on the full outer surface of a round tube whereas the double and vapor-chamber fin-tube geometries are calculated using the projected area of the tube block, which is always less. It is also seen that the armor thickness decreases with decreasing δ_s/δ_a since the projected area of the tube block decreases as the side-wall armor protection thickness decreases.

The radiator fin-tube L/R_o ratio obtained for maximum heat rejection per unit weight for the vapor-chamber, double, and central fin-tube geometries is shown plotted in figure 25 for the two power level cases. It is seen that the vapor-chamber fin-tube geometry has the largest value of L/R_o ratio over the entire range of tube inside diameters considered. The L/R_o ratio was also seen to increase with increasing tube inside diameter for all three geometries. The L/R_o ratio also increases for the double fin-tube geometry as the δ_s/δ_a ratio increases. This trend did not hold for the vapor-chamber fin-tube geometry. Values of actual fin length ℓ for the vapor fin radiator can be obtained from the values of L/R_o in figure 25 in conjunction with the armor thickness δ_a (fig. 24), the ratio δ_s/δ_a , and equation (13).

DEGRADATION OF RADIATING EFFECTIVENESS

It was specified arbitrarily in the analysis of the vapor-chamber fin (appendix D) that 25 percent of the individual fin segments could be punctured by meteoroids. Upon puncture, the chamber working fluid, which is under pressure, would be lost and the fin would

no longer act as a vapor fin. However, the fin does not lose its radiating effectiveness entirely when punctured since it will then behave similar to a solid-conducting double fin (fig. 3(a)). The degradation of the total heat rejection capabilities of the radiator with punctured fins then becomes a function of the number of surviving segments and the thermal effectiveness of the punctured fin segment.

The actual physical case would require a complex two-dimensional analysis, since the fin surfaces of the punctured segment can also receive heat by conduction axially from the fin surface of adjacent unpunctured segments and by radiation from the bulk-heads of the segment (kept at temperature by the adjacent unpunctured segments). Thus the true radiating effectiveness would be expected to be greater than that indicated for the one-dimensional situation of figure 3(a).

The complexity of analyzing the actual physical case required an initial simplified approach that considers each punctured fin segment as a double fin tube and uses the one-dimensional analysis of reference 9 to obtain the new fin thermal efficiency. The characteristic fin length used in obtaining the fin efficiency is designated to be the minimum fin dimension. The minimum fin length depends on the value of fin segment aspect ratio ℓ/b , the fin segment planform area, and the arrangement of the punctured segments as shown in figure 26. For a single segment puncture, the minimum fin length will be b or 2ℓ ; and, for two adjacent fin segments punctured, the minimum fin length will be $2b$ or 2ℓ .

The degradation of radiating effectiveness can be expressed as the ratio of the radiator heat rejection after vapor fin puncture to the design heat rejection with no fin puncture. This expression is

$$\eta_D = \frac{(Q_{rej})_{\text{after puncture}}}{(Q_{rej})_{\text{design}}} \quad (17)$$

The heat rejection after puncture is comprised of (1) the vapor header heat rejection $Q_{VH} = (1 - X_{tf})Q_{rej}$, which is not affected; (2) the heat rejection from the vapor-chamber fins and tubes not punctured $Q_{rej}X_{tf}(N_s/N)$; and (3) the heat rejection of the fins that are punctured and assumed to act as a double solid-conducting fin-tube geometry according to

$$Q_{rej}X_{tf}\left(1 - \frac{N_s}{N}\right) = 4\sigma\epsilon\ell\left(\eta_f + \frac{R_b}{\ell}\right)\left(1 - \frac{N_s}{N}\right)N_TZT_b^4 \quad (18)$$

where the double fin thermal efficiency η_f is obtained by using the characteristic fin length associated with the punctured fin arrangement and the results of reference 9.

When using either the b or 2ℓ dimension for the characteristic fin length, it is assumed that the temperature of the adjacent hot chamber is maintained at the design value of T_f . It is further assumed for simplicity of calculation that the adjacent fin temperature is equal to the tube block side-wall temperature (e. g. , $T_f/T_b = 0.995$ for $h_B = h_C = 10^4$ Btu/(hr)(sq ft)($^{\circ}$ F), fig. 5).

Figure 27 shows a plot of thermal radiating effectiveness against fin segment planform area for the two power levels chosen for the comparisons. It is seen from the curves for the 1-megawatt beryllium case that the thermal effectiveness of a single punctured fin (given by the $b, 2\ell$ curve) decreases sharply with increasing fin segment planform area until b equals 2ℓ , at which point the thermal effectiveness begins to slowly increase once again. When two adjacent fin segments are punctured (given by the $2b, 2\ell$ curve) the thermal effectiveness decreases and then increases in a manner similar to the single puncture case with the exception that the $2b = 2\ell$ point occurs at a fin segment planform area one-half of that obtained for the single punctured fin $b = 2\ell$ point.

The curves obtained for the 500-kilowatt columbium case follow the same pattern as for the 1-megawatt beryllium case with the exception that the thermal effectiveness is decreased by 2 percent at the lower power level. This is brought about by the smaller fin thickness and the lower thermal conductivity of the 500-kilowatt columbium case.

As indicated previously, the thermal effectiveness of the real two-dimensional case would be higher than the results of the one-dimensional approximation given in figure 27.

CONCLUDING REMARKS

It has been shown in the analysis presented herein that, for the two sample high-temperature Rankine cycle direct-condensing radiators considered with a tube meteoroid nonpenetration probability of 0.995, the vapor-chamber fin-tube radiator can have a substantially lighter specific weight than both the central fin-tube and double fin-tube radiators, depending on the required tube block side-wall thickness and fin segment planform area. For example, for the 500-kilowatt-cycle columbium radiator case, the vapor-chamber fin-tube radiator can be from 45 to 60 percent lighter than the central fin radiator and from 35 to 40 percent lighter than the double fin radiator. For the 1-megawatt-cycle beryllium radiator case, the vapor-chamber fin-tube radiator can be from 40 to 50 percent lighter than the central fin radiator and from 30 to 33 percent lighter than the double fin radiator. Lower values of meteoroid nonpenetration probability and radiator redundancy would tend to reduce the relative difference obtained but would give smaller absolute values of specific weight.

The vapor-chamber fin-tube radiator was also shown to have a substantially smaller (13 to 18 percent) planform area, fewer number of radiator tubes, and larger tube inner

diameters than the other two fin-tube geometries at maximum heat rejection per unit weight. Furthermore, the temperature of the vapor fin, being uniform and near the value of the tube block temperature, may minimize any thermal stress problems associated with large temperature gradients in the fins of the solid-conducting-type geometries.

The unique construction features of the vapor-chamber fin-tube geometry enable a fin segment to function as a solid-conducting configuration after puncture by meteoroids. One-dimensional calculations indicated that a maximum 12 to 14 percent reduction in radiating effectiveness occurred at maximum heat rejection per unit weight for the two power level cases investigated for 75 percent of the fin segments surviving without puncture. The actual degradation is expected to be less.

The weight, geometry, and thermal stress advantages of the vapor-chamber fin tube have to be weighed against the disadvantages of complexity of construction of the individual fin segments along with the associated problems of internal corrosion, sealing, and dependable operation of the fluid transport and heat-transfer characteristics within the chamber. Nevertheless, these preliminary results warrant further investigation into the merits of employing the vapor-chamber fin-tube concept for space radiator applications for other design conditions involving type of power cycle, power level, working fluid, temperature level, panel configuration, and nonpuncture probability. Investigation of vapor-chamber internal operating characteristics and limitations is also indicated.

Lewis Research Center,
National Aeronautics and Space Administration,
Cleveland, Ohio, February 18, 1965.

APPENDIX A

SYMBOLS

A	area, sq ft	K_H	fluid turning loss factor from header to tubes
A_p	radiator planform area, sq ft	k	thermal conductivity, Btu/(ft)(hr)(°F)
A_{seg}	fin segment planform area, sq ft	L	minimum half length of fin between tubes, ($L^* - R_o$), ft
A_v	vulnerable area for meteoroid protection, sq ft	L^*	one half tube center to center distance, ft
a	penetration relation correction factor	L_C	condensation tube length, ft
b	fin segment width, ft	ℓ	half length of fin between tubes, $L + [1 - (\delta_s/\delta_a)]\delta_a$, ft
C_P	specific heat, Btu/(lb _m)(°F)	\dot{m}	capillary fluid mass flow rate per unit length of radiator tube, (lb _m)/(hr)(ft)
c	acoustic velocity in target material, $\sqrt{E_a g/\rho_a}$, ft/sec	N	number of fin segments
D	diameter, ft	N_s	number of fin segments not punctured in given time
E_a	Young's modulus of target material, lb _f /sq ft	N_T	number of radiator tubes
F	angle factor	n, φ, θ_p	exponents
g	gravitational constant, (lb _m)(ft)/(lb _f)(sec ²)	P	cycle fluid pressure, lb _f /sq ft
h	heat of condensation or vaporization, Btu/lb _m	ΔP	pressure drop, lb _f /sq ft
h_B	fin vapor boiling heat-transfer coefficient, Btu/(hr)(sq ft)(°F)	P_e	electrical power output, W
h_C	fin vapor condensing heat-transfer coefficient, Btu/(hr)(sq ft)(°F)	$P(0)$	probability of no critical damage to radiator tubes, headers, or fin segments
J	mechanical equivalent of heat, 778 (ft)(lb _f)/Btu	Q	heat rejection rate, Btu/hr
K	radiation distribution parameter, $(q_b + 2q_f)/\epsilon\sigma\pi D_i T_b^4$	Q_f	fin radiant heat rejection rate for half fin length ℓ radiating from both sides, Btu/hr

Q_{rej}	total radiator heat rejection rate, Btu/hr	X_{tf}	fraction of total heat rejected by tubes and fins
$Qual_3$	radiator inlet quality	X_{VH}	fraction of total heat rejected by vapor header
q	heat rejection rate per unit tube length, Btu/(hr)(ft)	Z	tube length, ft
R	radius, ft	α, β	experimentally observed constants for meteoroid mass distribution
R'	fraction of flow area occupied by one phase	δ_a	tube armor protection thickness, ft
R_b	tube side wall to tube center-line dimension, $R_o - [1 - (\delta_s/\delta_a)] \delta_a$, ft	δ_c	tube liner thickness, ft
Re	Reynolds number	δ_f	fin transverse bulkhead thickness, ft
S	probability of N_s or more segments not punctured in time τ	δ_s	tube side-wall thickness, ft
T	temperature, $^{\circ}R$	$(\delta_{VH})_c$	vapor header liner thickness, ft
T^*	static fluid temperature at tube inlet, $^{\circ}R$	$(\delta_{LH})_c$	liquid header liner thickness, ft
T_b	temperature of tube block outer surface, $^{\circ}R$	ϵ	surface total hemispherical emittance
T_f	average temperature of fin surface, $^{\circ}R$	η_D	degradation of radiating effectiveness, eq. (17)
T_s	average vapor temperature in fin chamber, $^{\circ}R$	η_f	fin efficiency
T_w	temperature of tube block side wall, $^{\circ}R$	η_R^*	total fin-tube effectiveness
t	thickness of fin outer wall, ft	λ	fin heat-transfer parameter, eq. (6b)
u	velocity of vapor, ft/sec	μ	viscosity of working fluid, $lb_m/(ft)(sec)$
V	velocity of liquid, ft/sec	ρ	density, $lb_m/cu\ ft$
V_p	average meteoroid velocity, ft/sec	$\rho_w \delta_w$	capillary material weight per unit area of surface, $lb_m/sq\ ft$
W	weight, lb_m	σ	Stefan-Boltzmann constant, $1.713 \times 10^{-9} \text{ Btu}/(sq\ ft)(hr)(^{\circ}R^4)$
\dot{W}	mass flow per tube, lb_m/sec	τ	mission time, days
w	panel width, ft		

Φ, χ Lockhart-Martinelli two-phase
flow parameters

Subscripts:

a tube armor

B boiling

b tube block surface

C condensing

c tube liner

F friction

f fin

g gas or vapor phase

i inside

\mathcal{L} liquid

LH liquid header

m momentum

o outside

p particle

t tube

tot total flow, liquid and vapor

VH vapor header

w tube block side wall

0 conditions at tube inlet

3 radiator inlet conditions

APPENDIX B

TUBE BLOCK TEMPERATURE RATIO

Since the tubes will have thick walls due to the armor required for meteoroid protection, a significant temperature drop will occur between the tube liner and the outer surfaces of the tube block. The relation between the block side surface temperature and the tube block outer surface temperatures is based on a simplified approach utilizing one-dimensional conduction.

The heat transmission by conduction to the outer surface of the tube block is assumed to go a length δ_a over a cross-sectional area $2R_b Z$. The expression is

$$Q_b = \frac{2R_b k}{\delta_a} (T^* - T_b)Z \quad (B1)$$

The heat transmission by conduction to the side surface of the tube block is given by the equation

$$Q_w = \frac{2k(R_o - t)}{\delta_a \frac{\delta_s}{\delta_a}} (T^* - T_w)Z \quad (B2)$$

Dividing both sides of equations (B1) and (B2) by tube length Z and combining the two expressions by eliminating T^* yield

$$\frac{T_w}{T_b} = 1 - \frac{q_b \delta_a}{2kT_b} \left(\frac{q_w}{q_b} \frac{\delta_a}{R_o - t} - \frac{1}{R_b} \right) \quad (B3)$$

Elimination of q_b in equation (B3) requires the definition of the amount of heat radiated from one side of the tube block's outer surface,

$$q_b = 2\sigma\epsilon R_b T_b^4 \quad (B4)$$

Substitution of equation (B4) into equation (B3) yields the expression

$$\frac{T_w}{T_b} = 1 - \frac{\sigma \epsilon \delta_a R_b T_b^3}{k} \left(\frac{q_w}{q_b} \frac{\frac{\delta_s}{\delta_a}}{R_o - t} - \frac{1}{R_b} \right) \quad (B5)$$

Equation (B5) describing the tube wall temperature ratio can be simplified by noting that $t \ll R_o$ and $\delta_c \ll R_i$, which, along with the definition

$$R_o = R_b \left[1 + \frac{1 - \frac{\delta_s}{\delta_a}}{\frac{R_o}{\delta_a} - \left(1 - \frac{\delta_s}{\delta_a} \right)} \right] = R_i + \delta_a \quad (B6)$$

can be used to eliminate R_b in equation (B5) to yield the equation

$$\frac{T_w}{T_b} = 1 - \frac{\sigma \epsilon \delta_a T_b^3}{k} \left[\frac{q_w}{q_b} \frac{\delta_s}{\delta_a} \left(\frac{\frac{R_i}{\delta_a} + \frac{\delta_s}{\delta_a}}{\frac{R_i}{\delta_a} + 1} \right) - 1 \right] \quad (B7)$$

The outer surface temperature T_b in the previous equations is determined by combining equations (B1) and (B4) to obtain

$$T_b + \frac{\sigma \epsilon \delta_a}{k} T_b^4 = T^* \quad (B8)$$

Equations (7), (B7), and (B8) thus permit an evaluation of the ratio of tube block surface temperatures T_w/T_b . Plots of T_w/T_b against the heat ratio q_w/q_b are presented in figure 28 for three values of δ_s/δ_a by using a set of geometry inputs and material constants typical of the examples considered herein. These plots that are for typical 500-kilowatt columbium and 1-megawatt beryllium systems indicate that the tube block side-wall temperature T_w is not very different than the value of the tube block outer surface temperature T_b . Considering that, in practical configurations, values of q_w/q_b are of the order of 2 to 4 and values of δ_s/δ_a are likely to be near 0.5, it can be assumed that T_b and T_w are essentially equal for the class of examples treated herein. Thus T_w can be obtained from equation (B8).

APPENDIX C

PRESSURE DROP

Another factor that is required to determine the geometry and weight of a radiator is the allowable pressure drop in the radiator tubes and headers. This aspect of radiator design helps determine the vapor header geometry and the required tube diameter, tube length, and the number of tubes. The equations presented are for a Rankine cycle condenser radiator with assumed vapor quality in the vapor header equal to the vapor quality at the turbine exhaust, two-phase flow in the radiator tubes, and all-liquid flow in the liquid header. The detailed development of the equations given in this section are given in reference 8.

Vapor Header

The determination of the pressure drop in the vapor header is simplified by assuming that only the gas phase affects the pressure drop. This pressure drop is expressed as a ratio of ΔP to the header inlet pressure P_3 with the resulting ratio kept constant for comparative purposes. This equation for turbulent flow is

$$\left(\frac{\Delta P}{P_3}\right)_{VH} = \frac{0.00357 \rho_g u_{VH}^2}{2 P_3 Re^{0.2} D_{VH}} \quad (C1)$$

where u_{VH} is the uniform vapor velocity in the parabolic header (based on the turbine exhaust quality and neglecting the flow area occupied by the liquid), and Re is the vapor Reynolds number based on the vapor header maximum diameter D_{VH} . The value of D_{VH} is obtained from the expression

$$D_{VH} = \left[\frac{2 \dot{W} (Qual_3)}{\rho_g \pi u_{VH}} \right]^{1/2} \quad (C2)$$

and the total panel width w in equation (C1) is

$$w = \frac{N_T R_b}{2} \left(1 + \frac{\ell}{R_b} \right) \quad (C3)$$

The term $Qual_3$ in equation (C2) is the vapor quality at the entrance to the vapor header. The number of condensing tubes N_T in the previous equation is determined from the tube pressure drop analysis in conjunction with the optimization procedure used for this fin-tube geometry.

The amount of heat rejected to space from the parabolic vapor header is determined from the following expression:

$$Q_{VH} = Q_{rej} X_{VH} = 2.09 \sigma \epsilon D_{VH} F_{VH} w T_3^4 \quad (C4)$$

where the factor F_{VH} is defined as the vapor header view factor for radiant emission to space and given a value of 0.85 for this analysis (ref. 14).

Radiator Tubes

The pressure drop in the radiator tubes where flowing vapor is condensed was computed from a combination of several basic flow and energy equations that are given in detail in reference 8. The flow model used assumed that at any given section perpendicular to the flow direction, the temperature and pressure in both the liquid and vapor are uniform and the same for both phases. This flow model also assumed turbulent flow with liquid and vapor velocities uniform in each phase at a given cross section but that the two velocities were not necessarily equal. Pressure drops were computed for a series of incremental tube lengths, and the pressure drop for the whole tube was obtained by summing the incremental drops.

The total change in pressure for an entire radiator tube is comprised of a frictional and momentum component. The friction pressure drop is described by the expression

$$dP_F = -\Phi_g^2 Re_g^{1.8} \frac{0.092 \mu_g^2 dz}{g D_i^3 \rho_g} \quad (C5)$$

where $Re = 4\dot{W}_g / \pi D_i \mu_g$ and Φ_g is a function of χ . The differential form of the change in pressure due to a change in momentum is

$$-dP_m = \frac{1}{g \pi R_i^2} \left[d(\rho_g A_g V^2) + d(\rho_g A_g u^2) \right] \quad (C6)$$

A third relation is required that relates the increment of tube length and the increment of condensate formed

$$d\dot{W}_g = \frac{\frac{K\epsilon\sigma\pi D_i T_b^4}{3600} dZ + \frac{(C_P)_g \dot{W}_g + (C_P)_l \dot{W}_l}{Jh\rho_g} T dP_F}{h - \frac{V^2}{Jg} \left(1.5 - \frac{0.9 dR'_l}{d\chi} \frac{\chi \dot{W}_{tot}}{R'_l \dot{W}_g} \right) + \frac{u^2}{gJ} \left(1.5 - \frac{0.9 dR'_l}{d\chi} \frac{\chi \dot{W}_{tot}}{R'_l \dot{W}_g} \right) - \frac{(C_P)_g \dot{W}_g + (C_P)_l \dot{W}_l}{Jh\rho_g} T \frac{dP_m}{d\dot{W}_g}} \quad (C7)$$

where, for the vapor fin-tube radiator, the definition of K is

$$K = 4 \frac{R_b \eta^* R}{\pi D_i} \left(1 + \frac{\ell}{R_b} \right) \quad (C8)$$

Equations (C5), (C6), and (C7) along with equation (1) are solved simultaneously for $d\dot{W}_g$, dP_m , and dP_F . The total change in static pressure for each increment can then be found from the relation

$$dP = dP_m + dP_F \quad (C9)$$

and the total pressure change for the entire radiator tube can be found by summing the incremental changes. For comparative purposes, the total tube static pressure drop is expressed as ratio of pressure drop and the tube inlet pressure.

The pressure drop associated with the turning of the vapor from the vapor header into the radiator tubes and the acceleration of the flow in the tubes was calculated from the expression

$$\Delta P_{entrance} = K_H \frac{1}{2} \rho_g \frac{u_0^2}{g} \quad (C10)$$

where the tube entrance loss factor K_H is given the same value used in equation (7).

In order to find the length of tube required for condensation, equation (C7) is solved for dZ and numerically integrated until the vapor mass flow \dot{W}_g is reduced to zero. The integrated value of Z obtained when $\dot{W}_g = 0$ is then denoted as the condensation tube length L_C . An additional length of tube is required if subcooling of the condensate is specified (ref. 8).

Liquid Header

The pressure drop in the liquid header is obtained by applying Fanning's equation with a friction factor for turbulent flow. This expression is

$$\Delta P_{LH} = \frac{0.00102 \rho_{\mathcal{L}} V_{LH}^2 w}{D_{LH} Re_{\mathcal{L}}^{0.2}} \quad (C11)$$

where $Re_{\mathcal{L}}$ is the Reynolds number corresponding to the maximum liquid velocity V_{LH} which, in these calculations, was taken as 4 feet per second. The liquid header diameter D_{LH} , which is assumed constant, is determined by applying the continuity equation at the header exit to give the expression

$$D_{LH} = \left(\frac{N_T \dot{W}_{tot}}{\pi \rho_{\mathcal{L}} V_{LH}} \right)^{1/2} \quad (C12)$$

APPENDIX D

RADIATOR WEIGHT AND GEOMETRY

In analyzing the merits of the vapor fin-tube configuration in radiator designs, it is necessary to consider the ratio of total heat rejection per unit total weight Q_{rej}/W and the influencing effects of radiator geometry limitations on the maximum heat rejection per unit weight. It was important therefore, to determine the weights of the vapor and liquid headers as well as the tubes and fins.

Tube and Header Weight

In order to determine tube and header weight, the effects of meteoroid penetration must be considered. This will dictate the required armor protection thickness needed for the tube block δ_a . The tube block armor thickness is determined by using the meteoroid protection criteria given in reference 12, which is based on a comprehensive appraisal of the available data and theories concerning the meteoroid penetration phenomenon. According to reference 12, the resultant equation for the armor thickness δ_a is given by the expression

$$\delta_a = 2a \left(\frac{62.45 \rho_p}{\rho_a} \right)^{1/2} \left(\frac{V_p}{c} \right)^{2/3} \left(\frac{6.747 \times 10^{-5}}{\rho_a} \right)^{1/3} \left[\frac{\alpha A_v \tau}{-\ln P(0)} \right]^{1/3\beta} \left(\frac{1}{\beta + 1} \right)^{1/3\beta} \quad (D1)$$

where

- a 1.75 (for no puncture)
- ρ_p 0.44 g/cc
- V_p 98,400 ft/sec
- α $0.53 \times 10^{-10} g^\beta / (\text{sq ft})(\text{day})$ (ref. 15)
- β 1.34

Insertion of the aforementioned constants into equation (D1) along with utilizing Young's modulus in the definition of sonic velocity of the material yield the more compact form

$$\delta_a = \frac{1.48}{\rho_a^{1/6} E_a^{1/3}} \left[\frac{A_v \tau}{-\ln P(0)} \right]^{0.249} \quad (D2)$$

The total exposed area to be protected by direct impacts A_v , is assumed to be the outer surface of the vapor header and the projected area of the tube block. The liquid header contribution is assumed to be negligible, since its surface area is small compared to that of the vapor header. Thus

$$A_v = A_t + A_{VH} \quad (D3)$$

The projected area of the tube block is given by the expression

$$A_t = 4R_b N_T Z \quad (D4)$$

The value of the total tube length $N_T Z$ in equation (D4) is obtained from the total fin-tube effectiveness (eq. (12)), which is solved for $N_T Z$ and given as

$$N_T Z = \frac{2(Q_f + Q_b)}{4\sigma\epsilon R_b \left(1 + \frac{\ell}{R_b}\right) T_b^4 \eta_R^*} \quad (D5)$$

Substitution of equation (D5) into (D4) and defining $2(Q_f + Q_b) = Q_{rej}(1 - X_{VH})$ yield the expression

$$A_t = \frac{Q_{rej}(1 - X_{VH})}{\sigma\epsilon T_b^4 \left(1 + \frac{\ell}{R_b}\right) \eta_R^*} \quad (D6)$$

The fraction of heat rejected by the vapor header is written in terms of the total heat rejection rate as given by equation (C4). The vulnerable area of the vapor header is assumed to be its full required surface area for heat rejection and is given as

$$A_{VH} = \frac{Q_{rej} X_{VH}}{\sigma\epsilon F_{VH} T_3^4} \quad (D7)$$

where F_{VH} is the view factor for the effect of the radiator panel on the heat rejection of the vapor header surface. This analysis uses a value of $F_{VH} = 0.85$.

Combining equations (D3), (D6), and (D7) yields the total vulnerable area

$$A_V = \frac{Q_{rej}}{\sigma \epsilon} \left[\frac{1 - X_{VH}}{\left(1 + \frac{\ell}{R_b}\right) \eta_R^* T_b^4} + \frac{X_{VH}}{F_{VH} T_3^4} \right] \quad (D8)$$

where T_b is a function of T_3 and obtained from equations (7) and (B8), and η_R^* is obtained from the results of equation (12).

With the tube and header armor thickness determined, the weights of the tube block and headers can be written. The vapor header weight as given by reference 8 is modified by noting $w \gg (\delta_{VH})_c$ and $w \gg \delta_a$. This results in the expression

$$W_{VH} = \frac{4\pi w}{3} \left\{ [D_{VH} + (\delta_{VH})_c] (\delta_{VH})_c \rho_c + [D_{VH} + 2(\delta_{VH})_c + \delta_a] \delta_a \rho_a \right\} \quad (D9)$$

and that of the liquid header and condensate by reference 8

$$W_{LH} = 4\pi w \left\{ \frac{\rho_c D_{LH}^2}{4} + \rho_c (\delta_{LH})_c [D_{LH} + (\delta_{LH})_c] + \rho_a \delta_a [D_{LH} + 2(\delta_{LH})_c + \delta_a] \right\} \quad (D10)$$

The weight of the tube liner and armor block is given by the expression (ref. 9)

$$W_t = N_T Z \rho_a [4R_o R_b - \pi(R_i + \delta_c)^2] + \rho_c \pi Z N_T \delta_c (2R_i + \delta_c) \quad (D11)$$

In equation (D11) the weight of the liquid inventory in the subcooler portion of the radiator tubes is neglected since the subcooler length is small.

Fin Chamber Weight

Since the fin chamber for this configuration contains a fluid under its saturation pressure, meteoroid protection will be required on the entire fin outer surface. If the fin chamber were a single unit, the vulnerable area of the fin would be extremely large, thus requiring a heavy armor thickness and subsequent weight penalty. In order to reduce the armor requirement, as indicated earlier, the fins are segmented into a large number of sealed compartments (fig. 1).

The method of reference 16 was used to determine the manner in which segmenting might be used to obtain minimum fin weight for a specified probability that a certain fraction of the segments will remain unpunctured at the completion of the mission. The relation used states that, if the probability of not being punctured for each of N identical segments is $P(0)$, then the probability S of having N_s or more segments not punctured during the radiators useful life is given by the expression

$$S = \sum_{n=N_s}^N \frac{N!}{n! (N-n)!} [1 - P(0)]^{N-n} P(0)^n \quad (D12)$$

The proportion of segments surviving to total segments N_s/N was arbitrarily taken as 0.75. This value results in near minimum fin weight (ref. 16). Thus the individual segment probability $P(0)$ can be obtained from equation (D12) for a specified value of overall survival probability S and the number of fin segments desired.

Calculated values obtained from this analysis are given in figure 29 for individual segment probability against number of surviving segments for one value of overall fin segment nonpenetration probability that 75 percent of the segments will survive.

The total number of fin segments N was obtained from the ratio of total vapor fin planform area to planform area of a single segment.

$$N = \frac{(A_p)_f}{A_{seg}} \quad (D13)$$

The fin planform area in equation (D13) is determined from the expression

$$(A_p)_f = 2\ell N_T Z = \frac{Q_{rej}(1 - X_{VH})}{2\sigma\epsilon \left(1 + \frac{R_b}{\ell}\right) T_b^4 \eta_R^*} \quad (D14)$$

The surviving number of fin segments can be determined by combining equations (D13) and (D14) along with $N_s/N = 0.75$ to obtain

$$N_s = \frac{0.75 Q_{rej}(1 - X_{VH})}{2A_{seg} \epsilon \sigma \left(1 + \frac{R_b}{\ell}\right) T_b^4 \eta_R^*} \quad (D15)$$

Once N_s has been calculated for a given value of segment planform area A_{seg} , the probability of survival of an individual segment $P(0)$ is obtained from figure 29. By using this survival probability, the fin thickness for no puncture can be calculated from the expression (similar to eq. (D2)).

$$t = \frac{1.48}{\rho_a^{1/6} E_a^{1/3}} \left[\frac{2A_{seg}^7}{-\ln P(0)} \right]^{0.249} \quad (D16)$$

Meteoroid particles and distribution constants used in equation (D16) are the same as those used in equation (D2).

Upon obtaining values for fin thickness t and the total number of fin segments N , the vapor fin weight can be calculated using the following expression

$$W_f = 4N_T Z \left[\ell(\rho_f t + \overline{\rho_w \delta_w}) + (R_o - t) \overline{\rho_w \delta_w} \right] + 4\rho_f \delta_f \ell (R_o - t)(N + N_T) \quad (D17)$$

where the term $\overline{\rho_w \delta_w}$ takes into account the additional weight of the capillary material required to transport the chamber fluid by capillary action. The weight of the transverse bulkheads that separate the fin into a number of compartments is given by the last term in equation (D17).

Weight Ratio

The total heat rejection per unit weight of a fin-tube radiator can be expressed as

$$\frac{Q_{rej}}{W} = \frac{\frac{Q_{rej}}{N_T Z}}{\frac{W}{N_T Z}} \quad (D18)$$

The total heat rejection is comprised of the amount radiated from both sides of the fin-tube panel, $Q_{rej}(1 - X_{VH})$ (eq. (D6)), and that radiated from the vapor header (obtained from eq. (C4)). Combining equations (C4) and (D6) along with the definition of A_t obtained from equation (D4) and dividing the results by the total tube length yields the expression

$$\frac{Q_{rej}}{N_T Z} = \sigma \epsilon R_b \left(1 + \frac{\ell}{R_b} \right) \left(4 \eta_R^* T_b^4 + 1.045 \frac{D_{VH} F_{VH} T_3^4}{Z} \right) \quad (D19)$$

The total weight of the radiator is comprised of the individual weights of the vapor header, liquid header, tube block, and fin chamber,

$$W = W_{VH} + W_{LH} + W_t + W_f \quad (D20)$$

The weight of the fin chamber heat-transport fluid can be included in the term for capillary weight $\rho_w \delta_w$ in equation (D17). Equation (D20) is obtained by summing the results of equations (D9) to (D11), and (D17). The denominator of equation (D18) can be found by dividing the total radiator weight by the total tube length $N_T Z$ obtained from the results of the optimization procedure. This result along with equation (D19) when inserted into equation (D18) yield the radiator heat rejection per unit weight. The peak value of Q_{rej}/W can then be obtained by plotting the results of equation (D18) as a function of the variables of interest.

Panel Geometry

In addition to the important aspect of minimizing weight for practical radiator designs, it is also of interest in most cases, to investigate the geometry of the radiator as it might affect the integrating of the vehicle and radiator. Planform area, aspect ratio, and fin thickness are three facets of geometry of the radiator panel that must be determined in order to satisfy radiator-space vehicle integration and structural and fabrication requirements of the fin-tube configuration.

Radiator planform area A_p is obtained from the equation

$$A_p = 2N_T Z (\ell + R_b) \quad (D21)$$

Substitution of equation (D5) into (D21) yields

$$A_p = \frac{Q_{rej}(1 - X_{VH})}{2\sigma \epsilon T_b^4 \eta_R^*} \quad (D22)$$

It is seen from equation (D22) that planform area will vary inversely with overall fin-

tube effectiveness η_R^* and therewith T_f/T_b for a specific choice of power and temperature level. The planform will generally increase with increasing ℓ/R_b because η_R^* decreases as ℓ/R_b is increased for fixed T_f/T_b .

Another important factor with respect to the geometry of the vapor fin-tube radiator is the magnitude of the fin thickness. Fin thickness is determined herein from meteoroid protection considerations according to equation (D16); however, the thickness should also be substantial enough to withstand thermal stresses, corrosion, and pressure differentials.

The panel aspect ratio, which is defined as the ratio of panel width w to tube length Z (fig. 1), is obtained by using equation (C3) for w and the results of the pressure drop calculations for Z .

REFERENCES

1. Krebs, R. P.; Winch, D. M.; and Lieblein, Seymour: Design and Optimization of Direct Condenser Radiators. Progress in Astronautics and Aeronautics. Vol. 11. Power Systems for Space Flight. Academic Press, Inc., 1963, pp. 475-504.
2. Denington, R.J., et al: Space Radiator Study. ER-4544, Thompson Ramo Wooldridge, Inc., 1962.
3. Haller, Henry C.; Wesling, Gordon C.; and Lieblein, Seymour: Heat-Rejection and Weight Characteristics of Fin-Tube Space Radiators With Tapered Fins. NASA TN D-2168, 1964.
4. Reynolds, W. C.: A Design-Oriented Optimization of Simple Tapered Radiating Fins. J. Heat Transfer (Trans. ASME) ser. C, vol. 85, no. 3, Aug. 1963, pp. 193-201; Discussion, pp. 201-202.
5. Hefner, R.J.: Design Procedure for a Minimum Weight Space Radiator. CF 60-8-21, Oak Ridge Nat. Lab., Aug. 1, 1960.
6. Sparrow, E. M.; and Minkowycz, W.J.: Heat Transfer Characteristics of Several Radiator Finned-Tube Configurations. NASA TN D-1435, 1962.
7. Haller, Henry C.: Comparison of Heat-Rejection and Weight Characteristics of Several Radiator Fin-Tube Configurations. NASA TN D-2385, 1964.
8. Krebs, Richard P.; Haller, Henry C.; and Auer, Bruce M.: Analysis and Design Procedures for a Flat, Direct-Condensing, Central Finned-Tube Radiator. NASA TN D-2474, 1964.
9. Haller, Henry C.: Analysis of a Double Fin-Tube Flat Condenser-Radiator and Comparison With a Central Fin-Tube Radiator. NASA TN D-2558, 1964.
10. Grover, G. M.; Cotter, T. P.; and Erickson, G. F.: Structures of Very High Thermal Conductance. J. Appl. Phys., vol. 35, no. 6, July 1964, pp. 1990-1991.
11. Final Report on Design Study for an Advanced Space Radioisotope Thermo-Electric Power Supply. General Atomic Report GA-5500, July 17, 1964.
12. Loeffler, I. J.; Lieblein, Seymour; and Clough, Nestor: Meteoroid Protection for Space Radiators. Progress in Astronautics and Aeronautics. Vol. 11. Power Systems for Space Flight. Academic Press, Inc., 1963, pp. 551-579.
13. Allingham, William D.; and McEntire, Jack A.: Determination of Boiling Film Coefficient for a Heated Horizontal Tube in Water-Saturated Wick Material. J. Heat Transfer (Trans. ASME), ser. C, vol. 83, no. 1, Feb. 1961, pp. 71-76.

14. Sparrow, E. M.; and Eckert, E. R. G.: Radiant Interaction Between Fin and Base Surfaces. J. Heat Transfer (Trans. ASME), ser. C, vol. 84, no. 1, Feb. 1963, pp. 12-18.
15. Whipple, Fred L.: On Meteoroids and Penetration. J. Geophys. Res., vol. 68, no. 17, Sept. 1, 1963, pp. 4929-4939.
16. English, Robert E.; and Guentert, Donald C.: Segmenting of Radiators for Meteoroid Protection. ARS J. vol. 31, no. 8, Aug. 1961, pp. 1162-1164.

TABLE I. - RELATIVE RADIATOR SPECIFIC WEIGHT
AT MAXIMUM HEAT REJECTION PER UNIT WEIGHT
[Mission time, 500 days; nonpenetration probability,
0.995; nonredundant.]

δ_s/δ_a	Fin-tube radiator			
	Vapor chamber		Double	Central
	Fin segment planform area, A_{seg} , sq in.			
	10	40	-----	----
500-Kilowatt-cycle columbium radiator				
0	0.381	0.405	0.608	1.0
.5	.524	.560	.894	
1-Megawatt-cycle beryllium radiator				
0	0.471	0.490	0.687	1.0
.5	.608	.628	.922	

TABLE II. - RELATIVE RADIATOR PLANFORM AREA
AT MAXIMUM HEAT REJECTION PER UNIT WEIGHT
[Mission time, 500 days; nonpenetration probability,
0.995; nonredundant.]

δ_s/δ_a	Fin-tube radiator		
	Double	Vapor chamber	Central
500-Kilowatt-cycle columbium radiator			
0	0.917	0.822	1.0
.5	.950	.848	
1-Megawatt-cycle beryllium radiator			
0	0.940	0.845	1.0
.5	.952	.877	

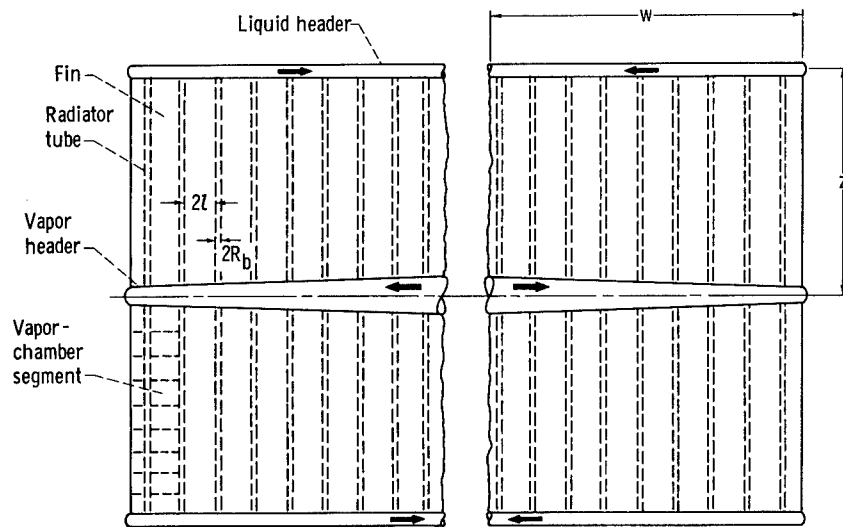


Figure 1. - Four-panel radiator with segmented vapor-chamber fins.

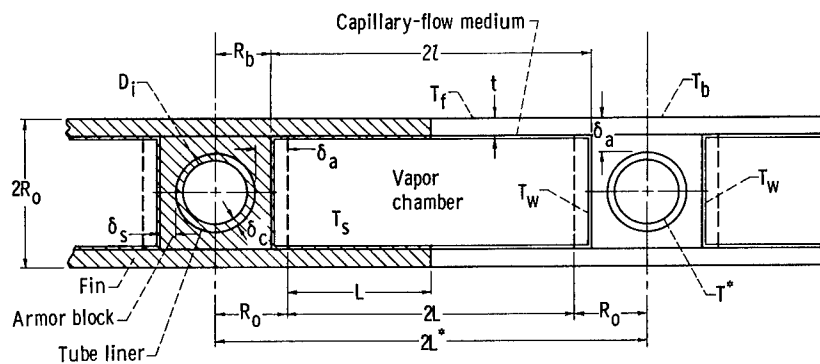
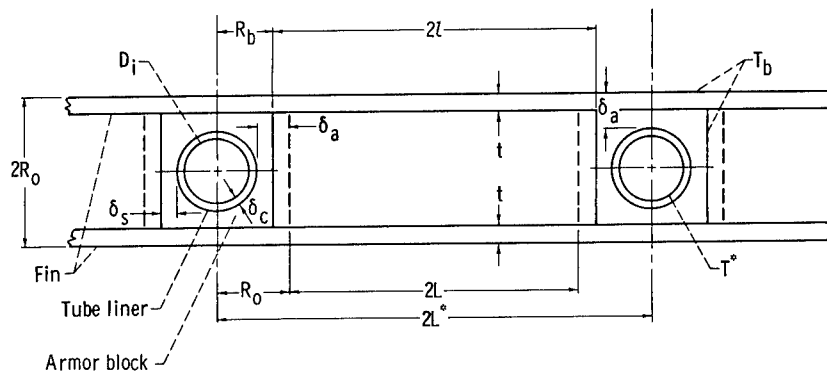
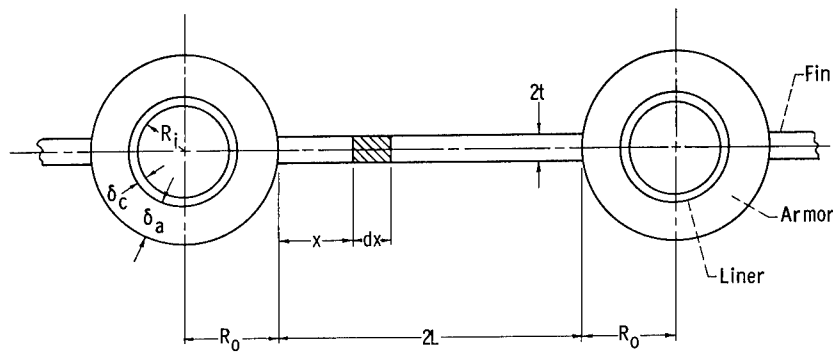


Figure 2. - Cross section of vapor-chamber fin-tube geometry.



(a) Double fin-tube geometry with variable tube block side-wall thickness.



(b) Central fin-tube geometry.

Figure 3. - Solid-conducting fin-tube geometries.

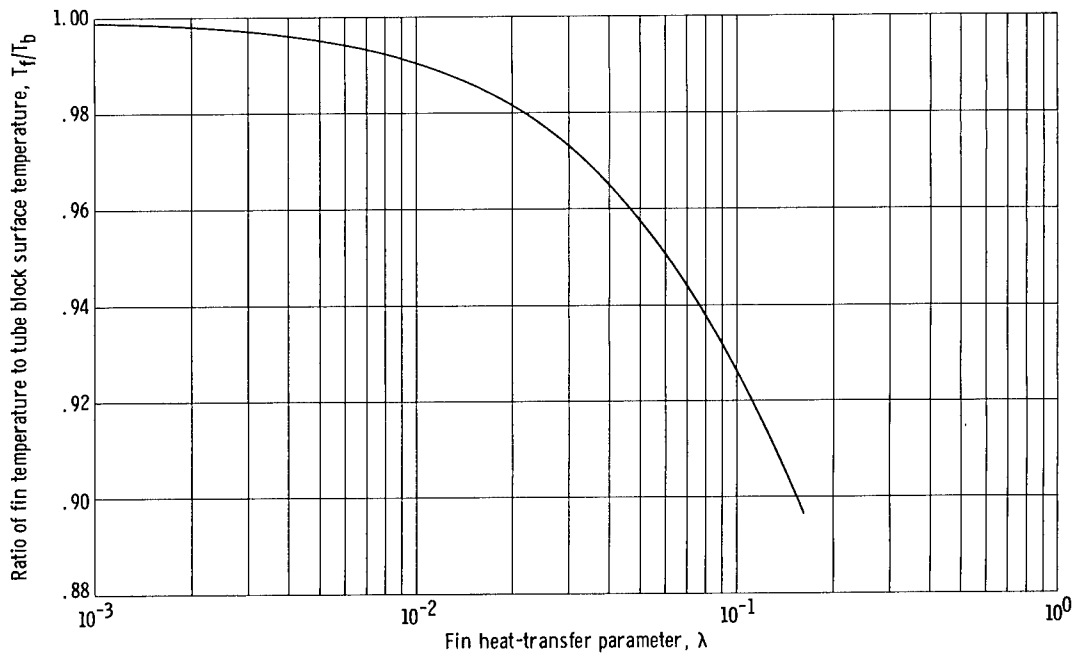
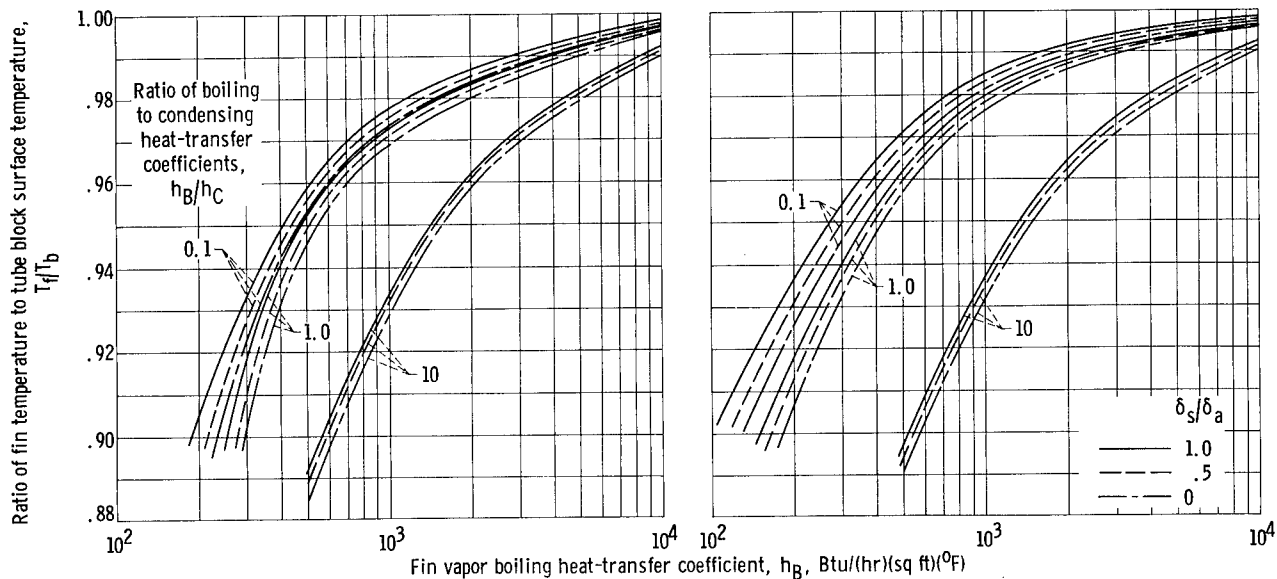


Figure 4. - Variation of ratio of fin temperature to tube block surface temperature with general fin heat-transfer parameter for vapor-chamber fin-tube geometry.



(a) Electrical power output, 500 kilowatts; columbium fins and tube armor; inside tube diameter, 0.50 inch; tube armor protection thickness, 0.0276 foot; minimum fin length, 0.162 foot.

(b) Electrical power output, 1 megawatt; beryllium fins and tube armor; inside tube diameter, 0.75 inch; tube armor protection thickness, 0.03152 foot; minimum fin length, 0.164 foot.

Figure 5. - Variation of ratio of fin temperature to tube block surface temperature with boiling heat-transfer coefficient for vapor-chamber fin-tube geometry. Radiator inlet temperature, 1700° R; static fluid temperature at tube inlet, 1623° R.

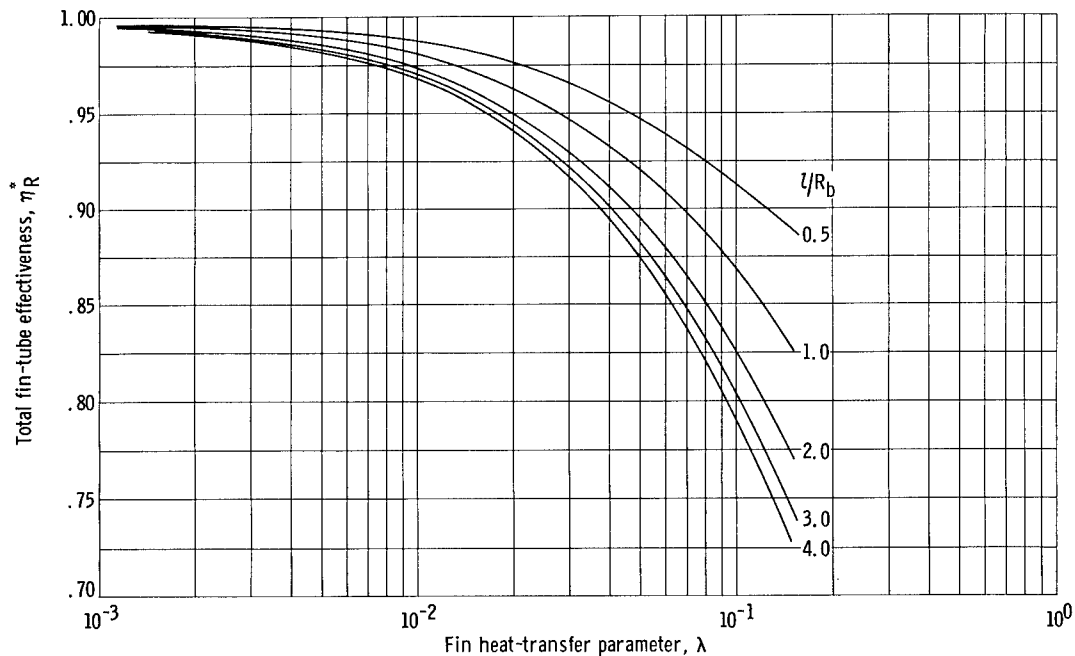


Figure 6. - Total vapor-chamber fin-tube effectiveness plotted against fin heat-transfer parameter.

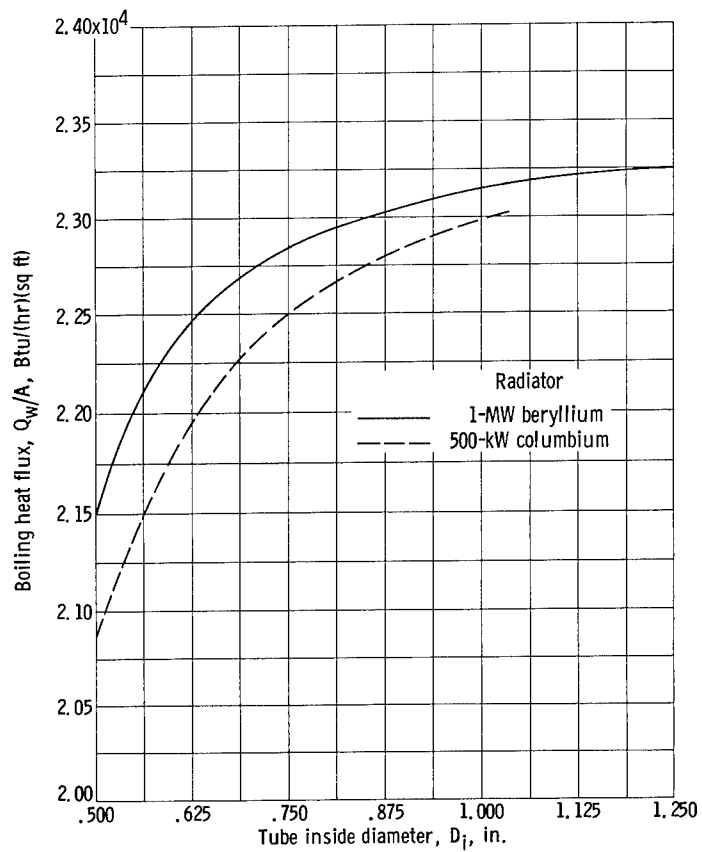


Figure 7. - Vapor-chamber fin capillary fluid boiling heat flux.

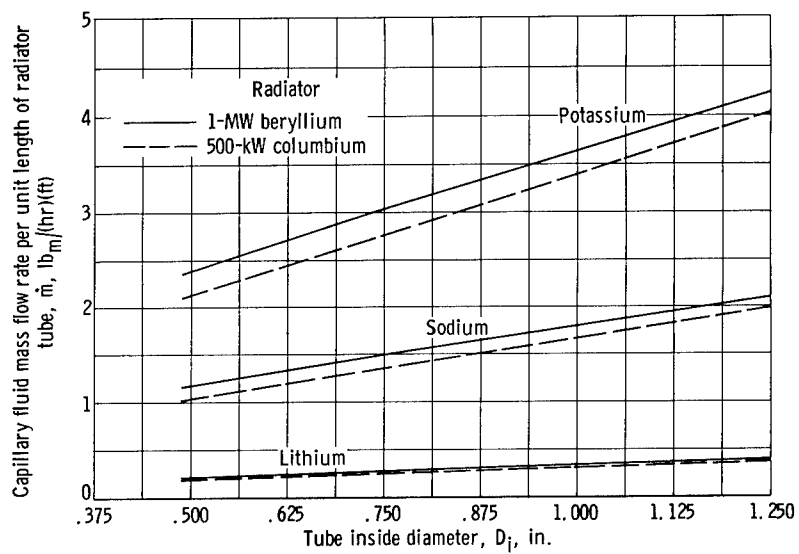
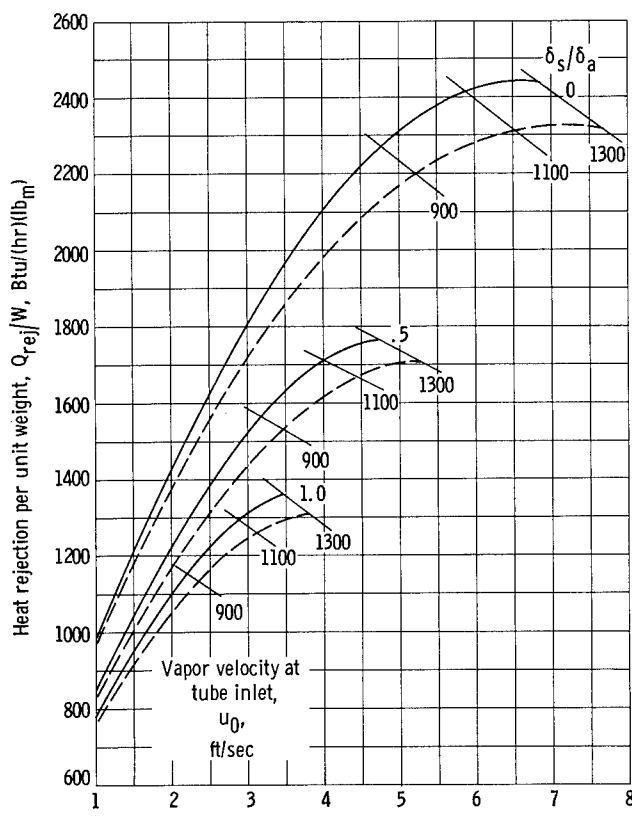
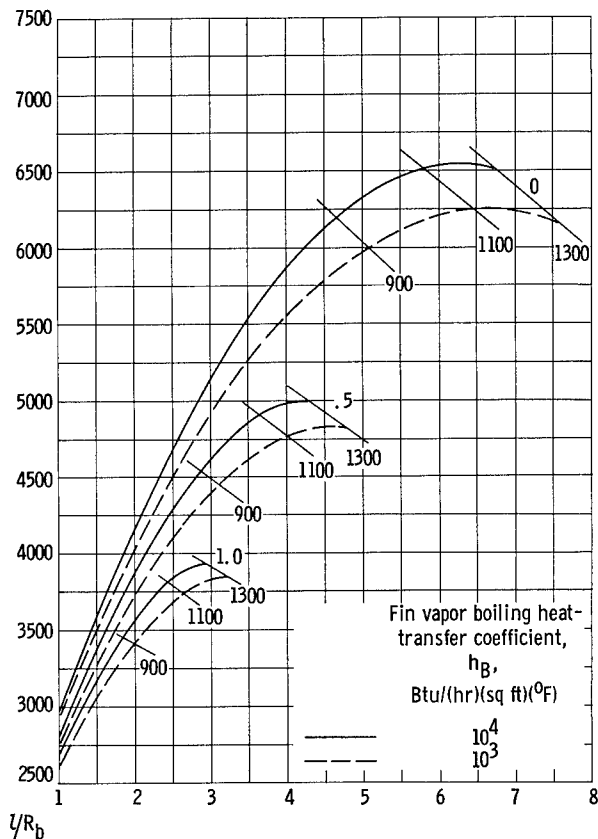


Figure 8. - Vapor-chamber fin capillary fluid flow rate.



(a) Electrical power output, 500 kilowatts; columbium fins and tube armor; capillary weight, 0.2 pound mass per square foot.



(b) Electrical power output, 1 megawatt; beryllium fins and tube armor; capillary weight, 0.1 pound mass per square foot.

Figure 9. - Ratio of heat rejection to weight for vapor-chamber fin-tube geometry. Radiator inlet temperature, 1700° R; inside tube diameter, 0.75 inch; fin segment planform area, 10 square inches; ratio of boiling to condensing heat-transfer coefficients, 1.0; fin overall survival probability, 0.900; tube nonpenetration probability, 0.995.

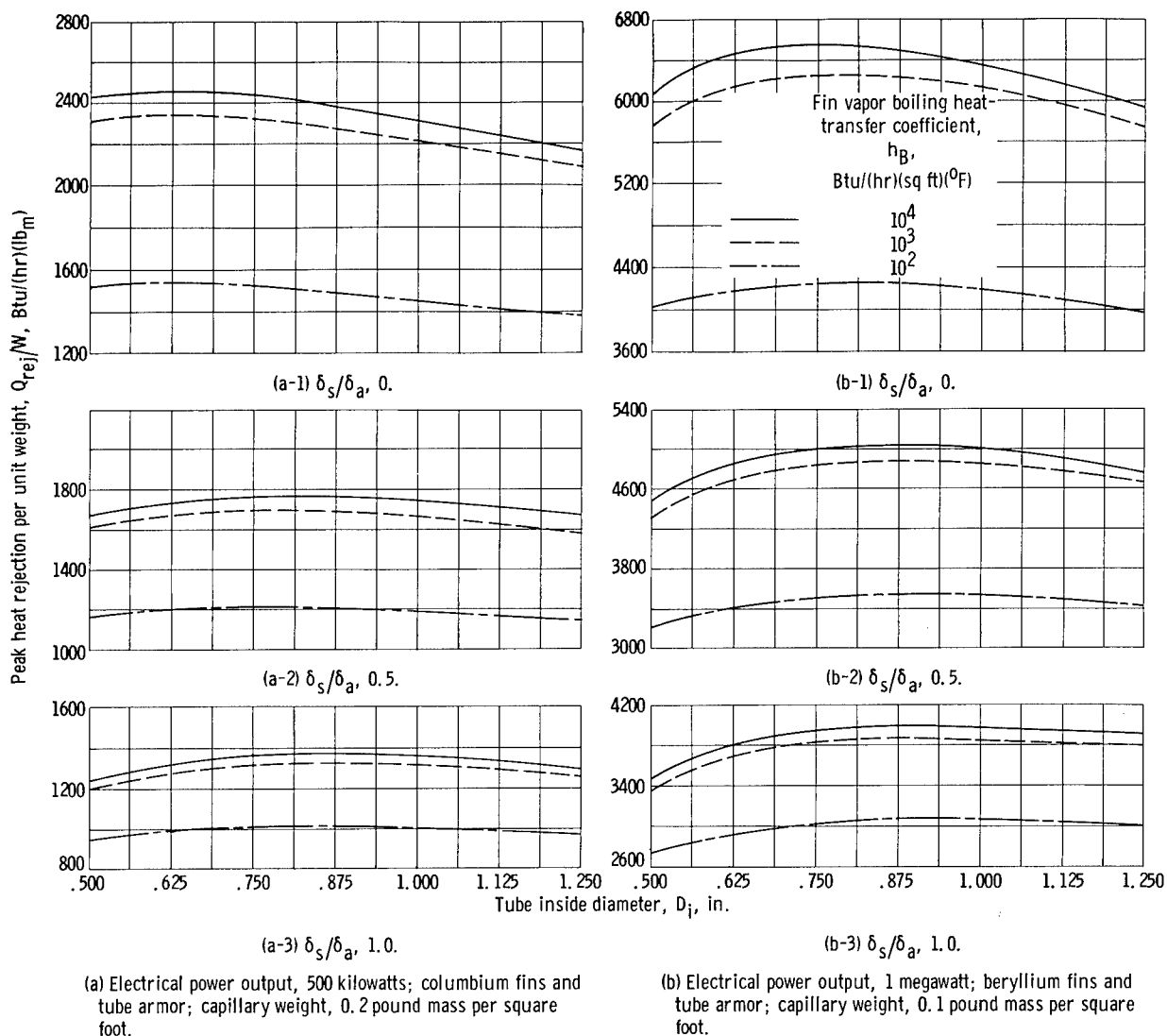


Figure 10. - Peak radiator heat rejection per unit weight for vapor-chamber fin-tube geometry. Radiator inlet temperature, 1700° R; fin segment planform area, 10 square inches; ratio of boiling to condensing heat-transfer coefficients, 1.0.

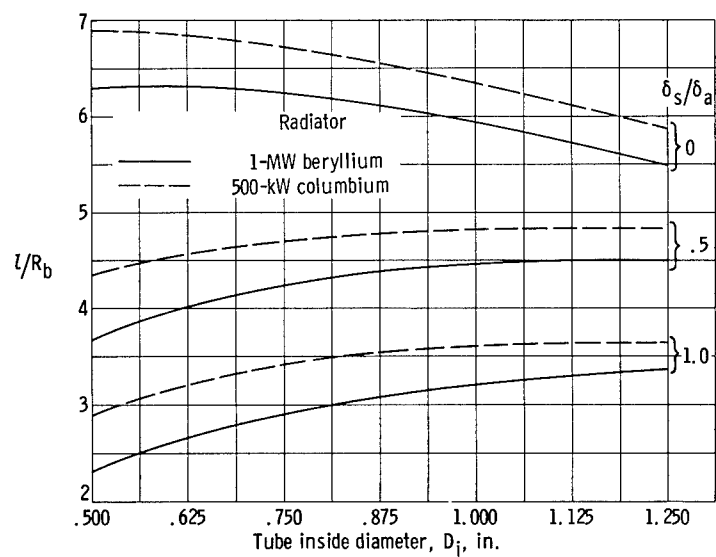
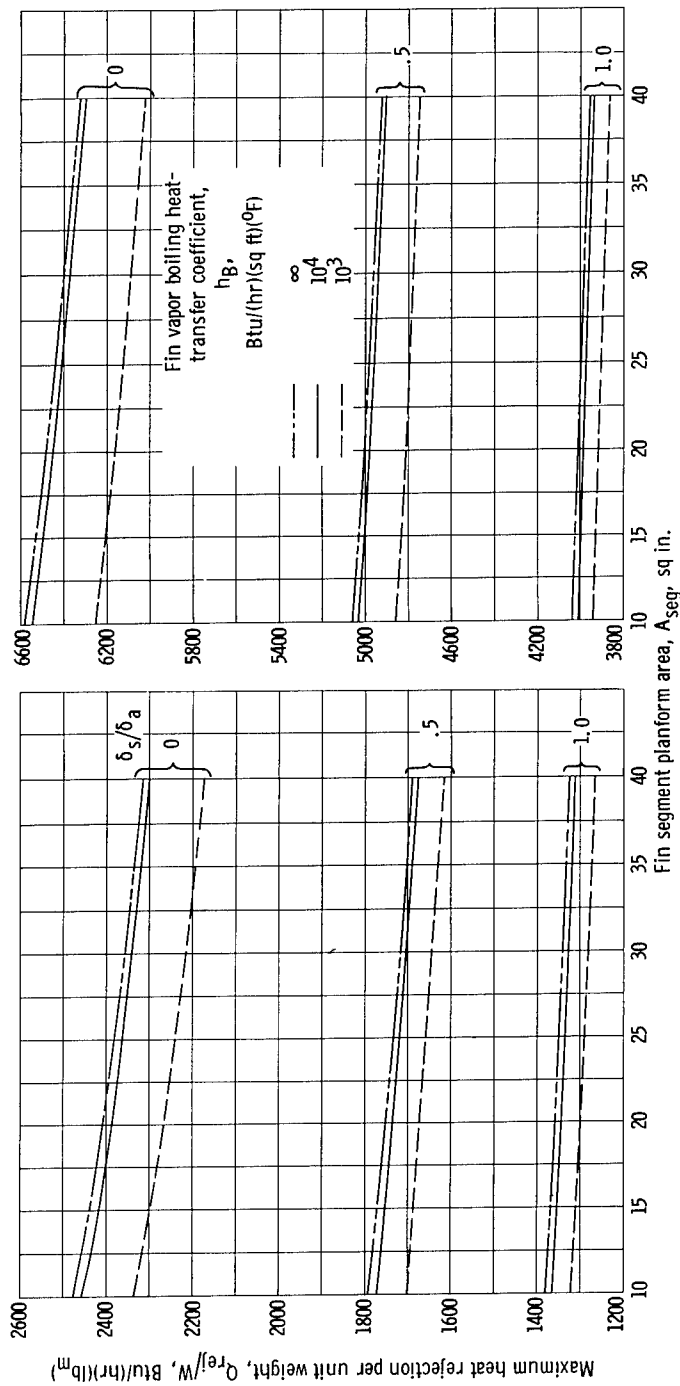


Figure 11. - Ratio of L/R_b at peak heat rejection per unit weight for vapor-chamber fin-tube geometry. Radiator inlet temperature, 1700°R ; fin segment planform area, 10 square inches; $h_B = h_C = 10^4$ Btu per hour per square foot per $^\circ\text{F}$.



(a) Electrical power output, 500 kilowatts; columbium fins and tube armor; capillary weight, 0.2 pound mass per square foot.
 (b) Electrical power output, 1 megawatt; beryllium fins and tube armor; capillary weight, 0.1 pound mass per square foot.

Figure 12. - Radiator maximum heat rejection per unit weight plotted against fin segment planform area for vapor-chamber fin-tube geometry. Radiator inlet temperature, 1700° R; ratio of boiling to condensing heat-transfer coefficients, 1.0.

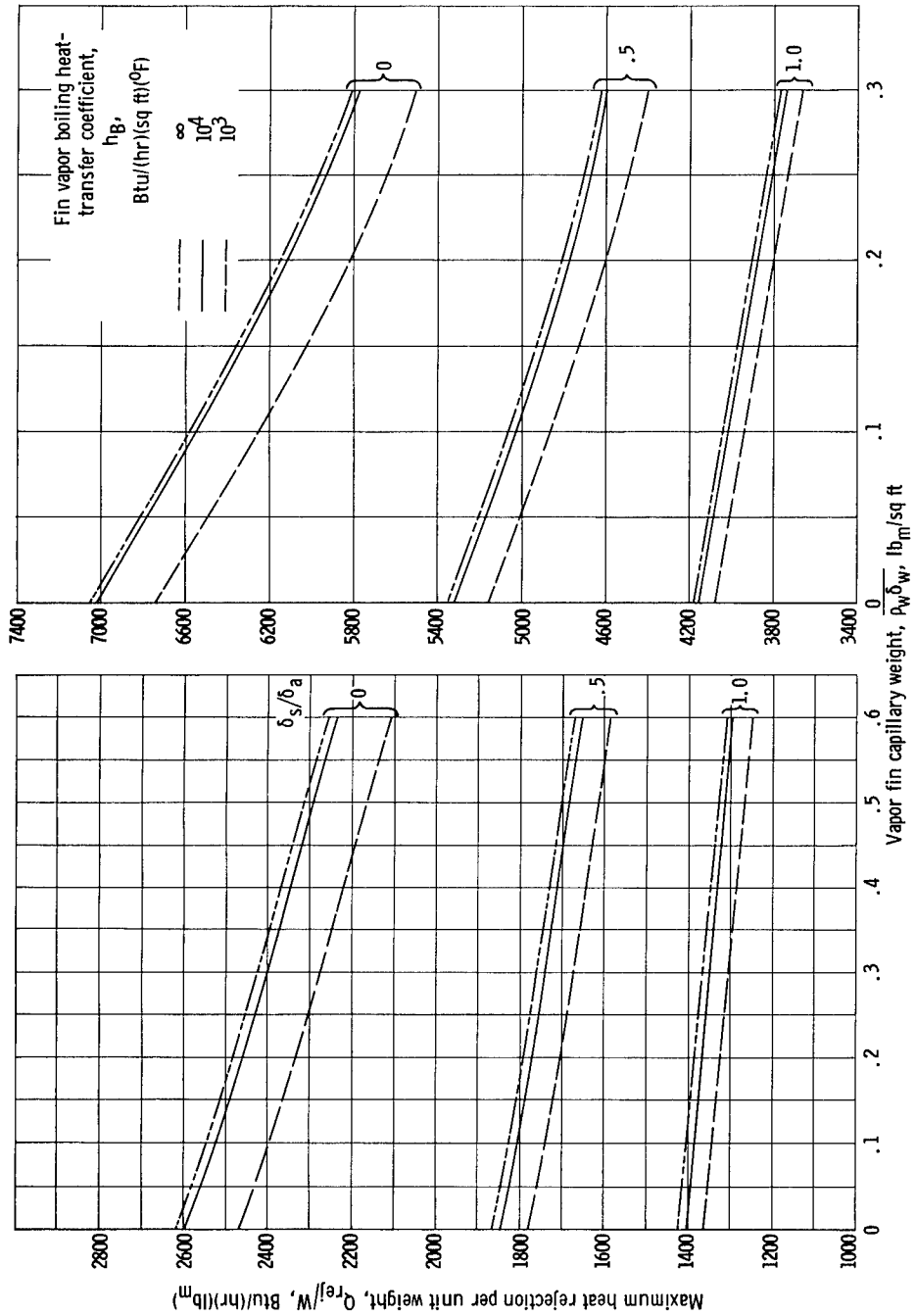
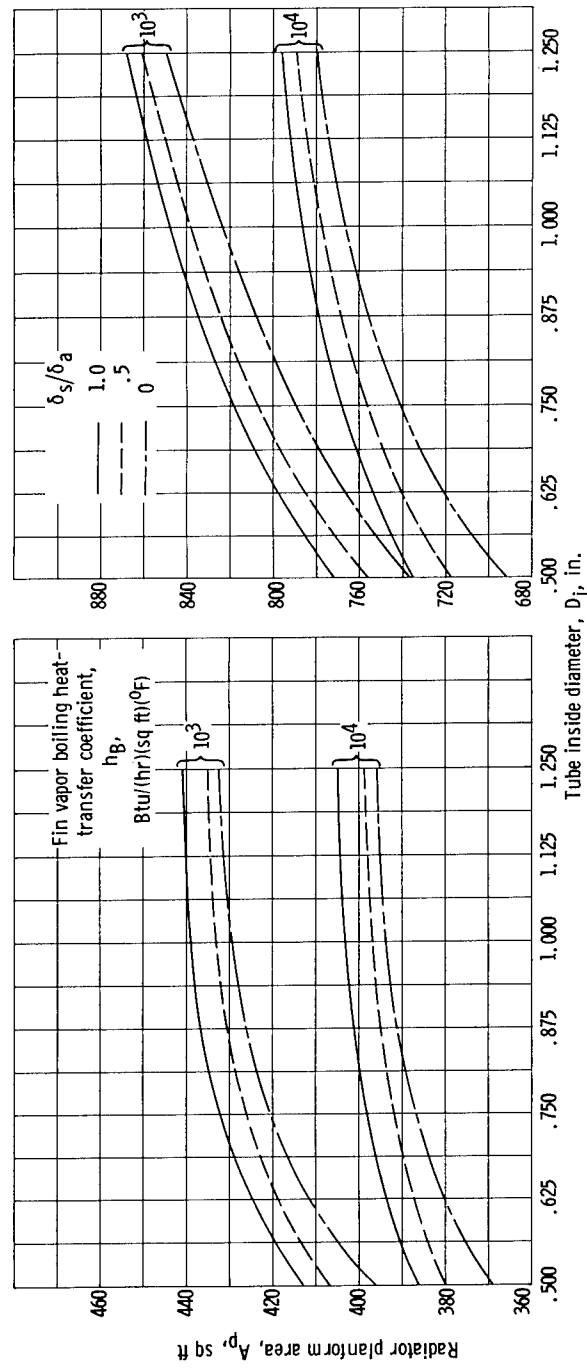


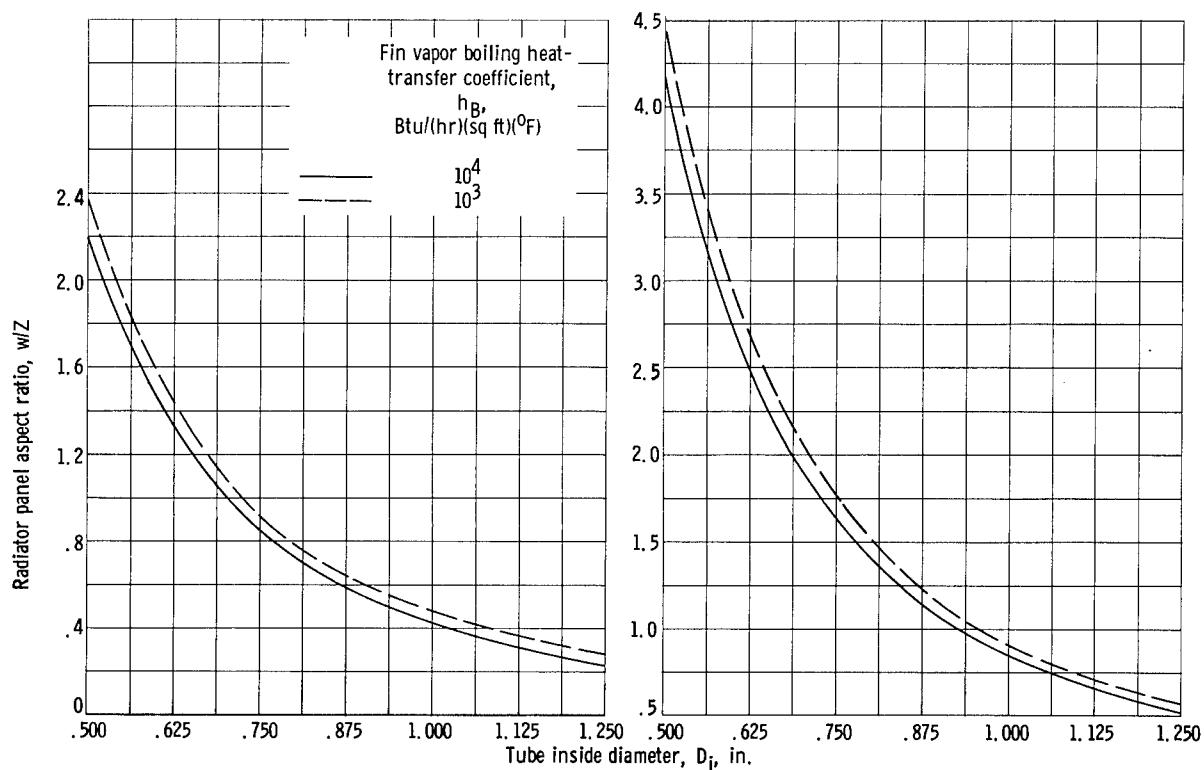
Figure 13. - Effect of vapor fin capillary material weight on radiator heat rejection per unit weight. Radiator inlet temperature, 1700°F ; fin segment planform area, 10 square inches; ratio of boiling to condensing heat-transfer coefficients, 1.0.



(a) Electrical power output, 500 kilowatts; columbium fins and tube armor; capillary weight, 0.2 pound mass per square foot.

(b) Electrical power output, 1 megawatt; beryllium fins and tube armor; capillary weight, 0.1 pound mass per square foot.

Figure 14. - Variation of radiator planform area with tube inside diameter at peak heat rejection per unit weight for vapor-chamber fin-tube geometry. Radiator inlet temperature, 1700° R; fin segment planform area, 10 square inches; ratio of boiling to condensing heat-transfer coefficients, 1.0.



(a) Electrical power output, 500 kilowatts; columbium fins and tube armor; capillary weight, 0.2 pound mass per square foot.

(b) Electrical power output, 1 megawatt; beryllium fins and tube armor; capillary weight, 0.1 pound mass per square foot.

Figure 15. - Variation of panel aspect ratio at peak heat rejection per unit weight for vapor-chamber fin-tube geometry. Radiator inlet temperature, 1700°R ; fin segment planform area, 10 square inches; ratio of boiling to condensing heat-transfer coefficients, 1.0; $\delta_s/\delta_a = 0.5$.

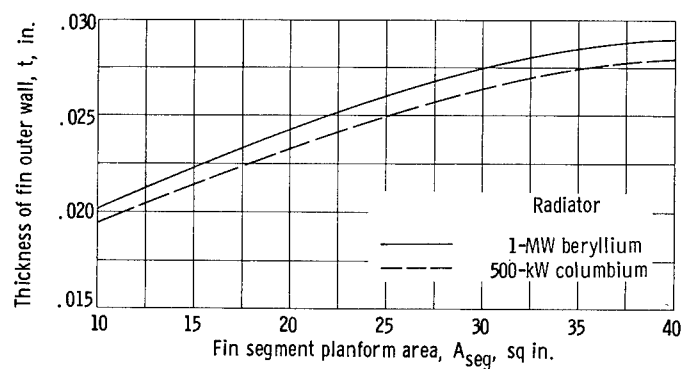


Figure 16. - Variation of fin thickness with fin segment planform area at maximum heat rejection per unit weight for vapor-chamber fin-tube geometry. Radiator inlet temperature, 1700°R ; $h_B = h_C = 10^4$ Btu per hour per square foot per $^{\circ}\text{F}$; $\delta_s/\delta_a = 0.5$.

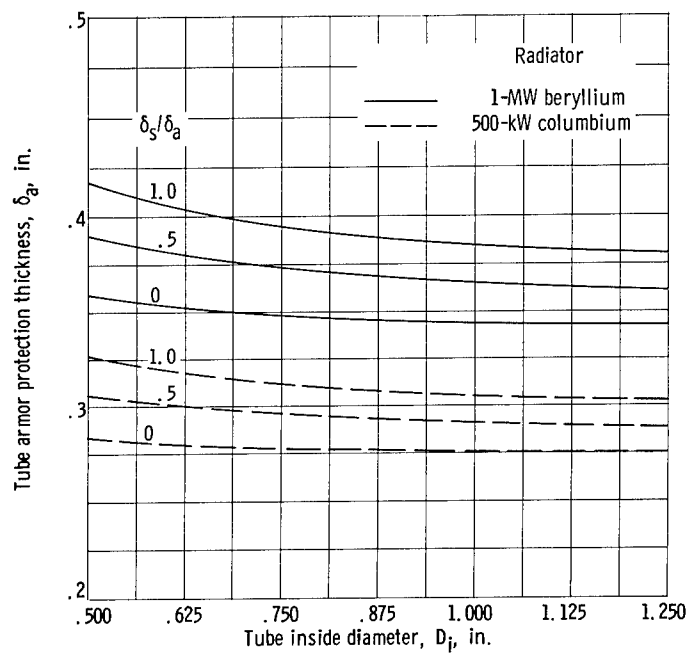


Figure 17. - Variation of maximum tube block armor thickness at peak heat rejection per unit weight with tube inside diameter for vapor-chamber fin-tube geometry. Radiator inlet temperature, 1700°R ; fin segment planform area, 10 square inches; $h_B = h_C = 10^4$ Btu per hour per square foot per $^{\circ}\text{F}$.

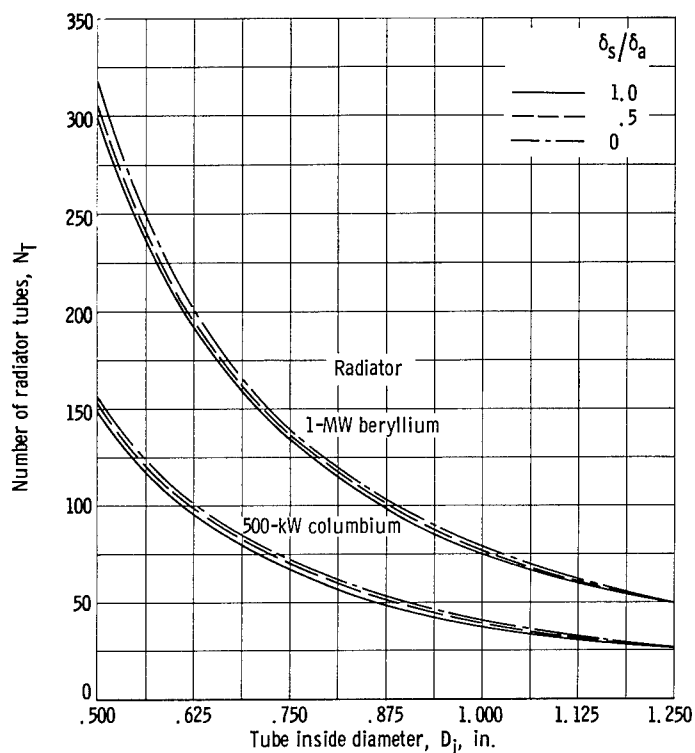


Figure 18. - Variation of number of radiator tubes with tube inside diameter at peak heat rejection per unit weight for vapor-chamber fin-tube geometry. Radiator inlet temperature, 1700°R ; fin segment planform area, 10 square inches; $h_B = h_C = 10^4$ Btu per hour per square foot per $^{\circ}\text{F}$.

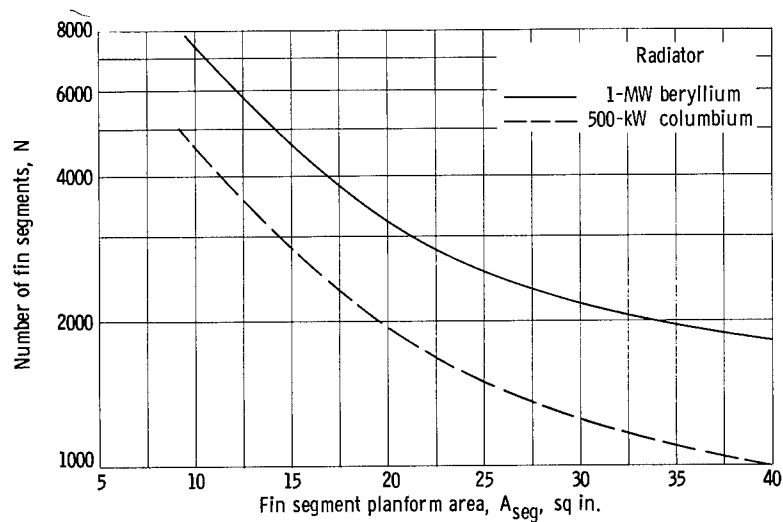


Figure 19. - Variation of number of fin segments with fin segment planform area.

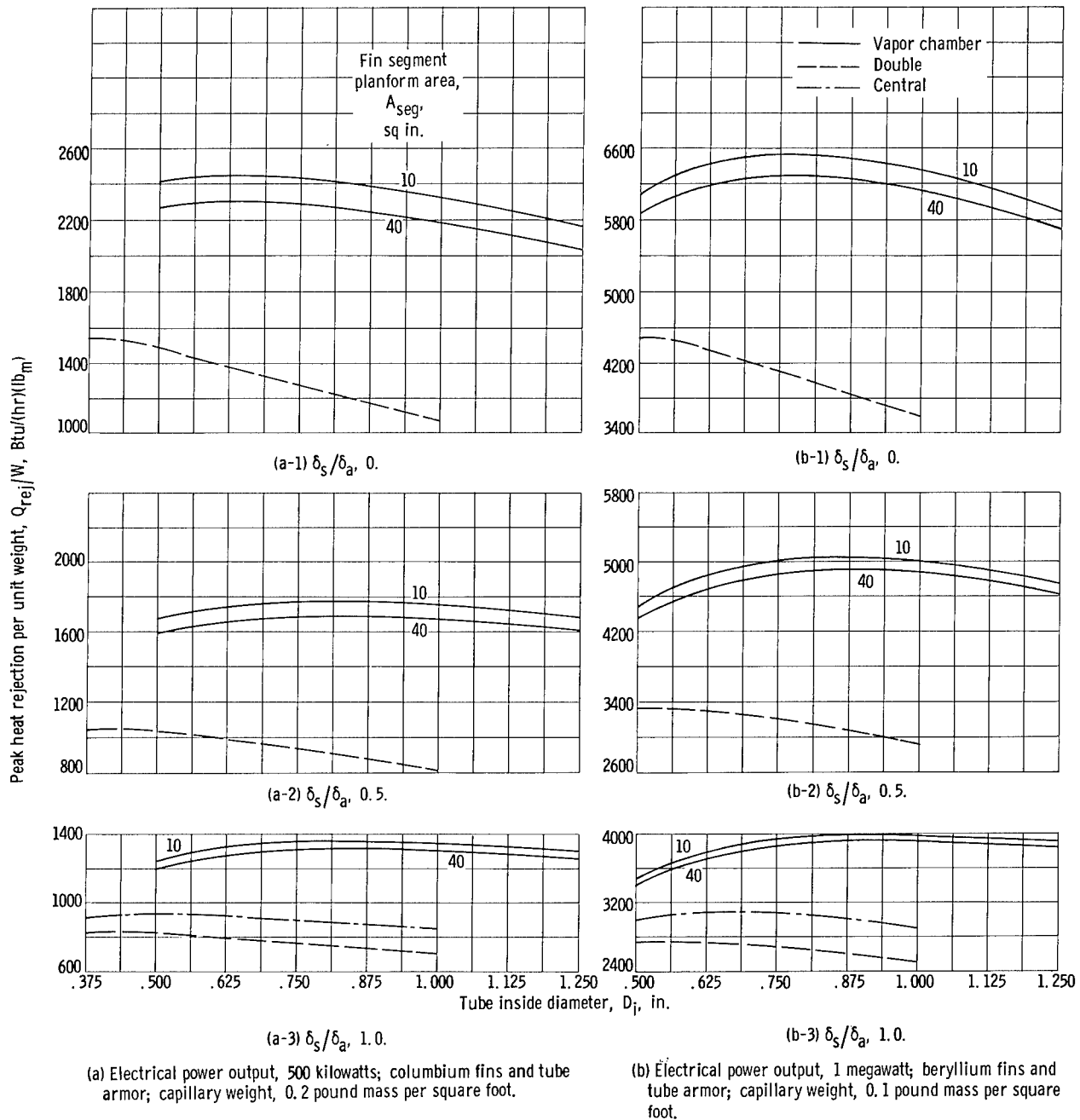


Figure 20. - Comparison of peak heat rejection per unit weight for vapor-chamber, double, and central fin-tube geometries. Radiator inlet temperature, 1700° R; $h_B = h_C = 10^4$ Btu per hour per square foot per °F.

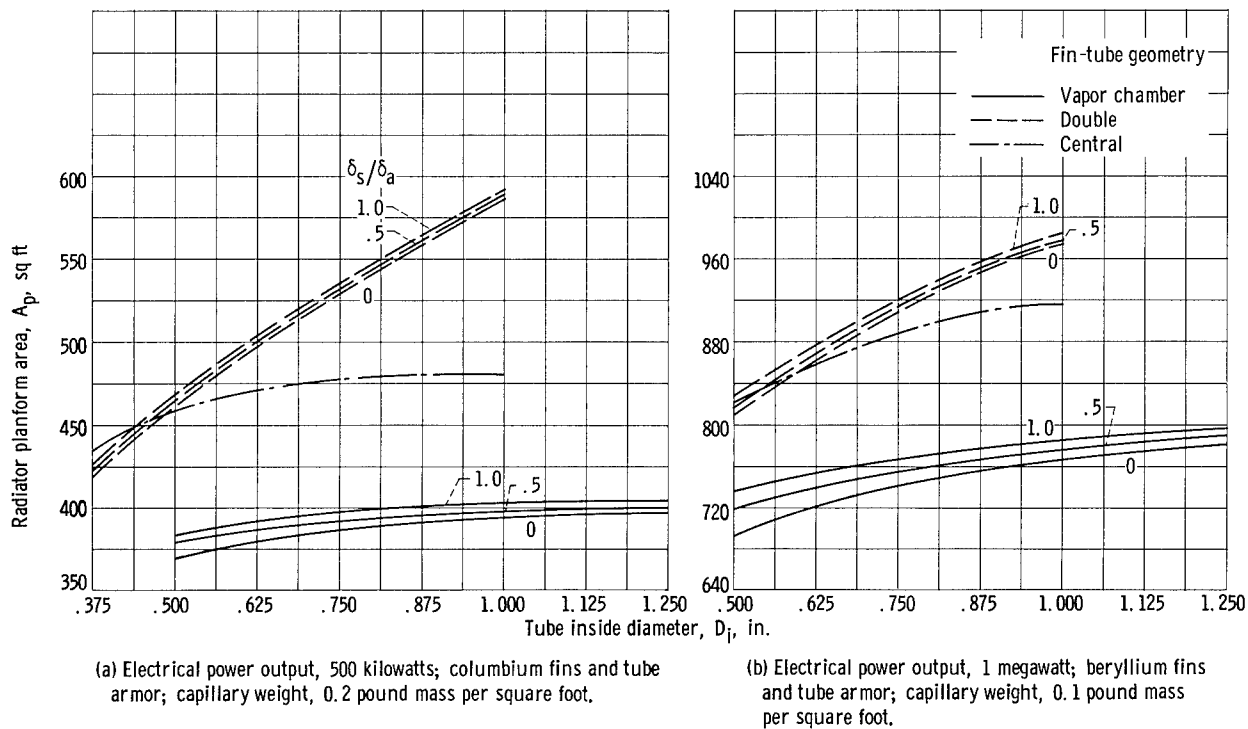


Figure 21. - Planform area comparison at peak heat rejection per unit weight for vapor-chamber, double, and central fin-tube radiators. Radiator inlet temperature, 1700°R ; fin segment planform area, 10 square inches; $h_B = h_C = 10^4$ Btu per hour per square foot per $^{\circ}\text{F}$.

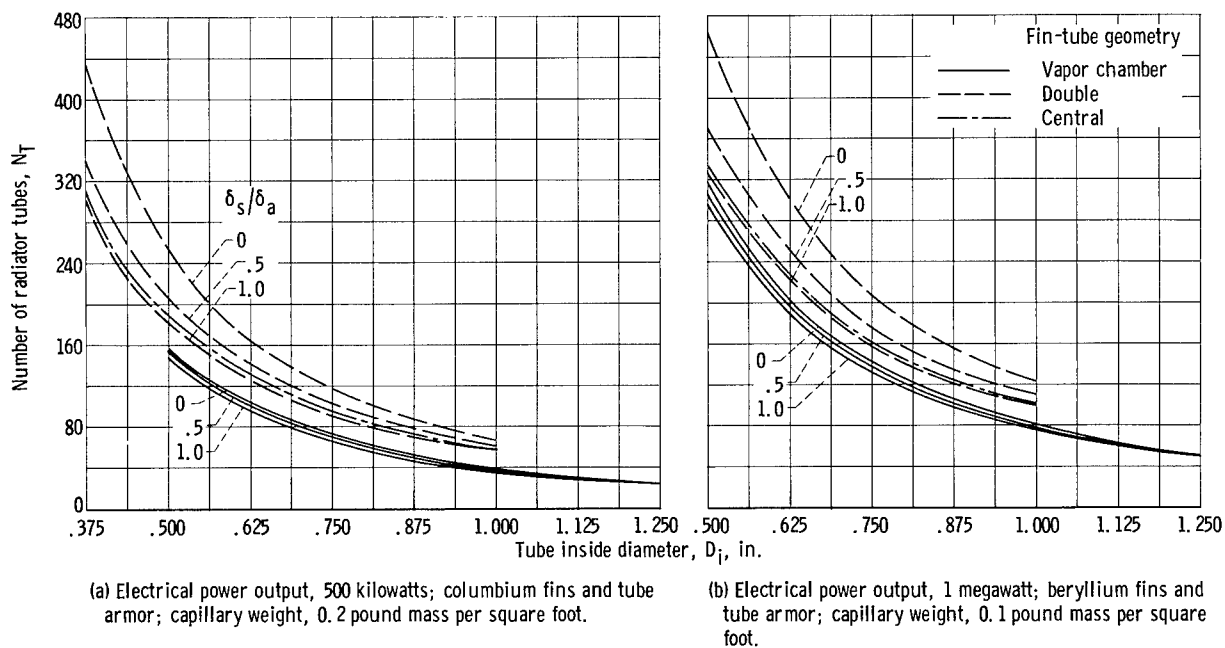
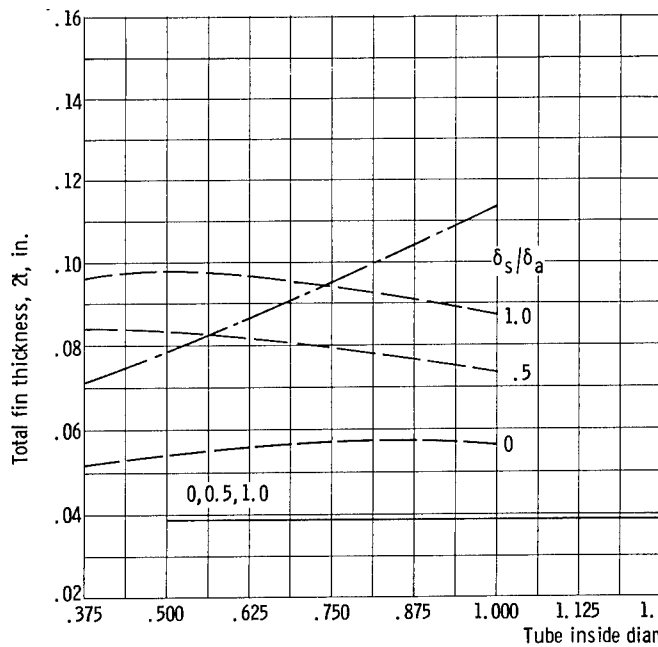
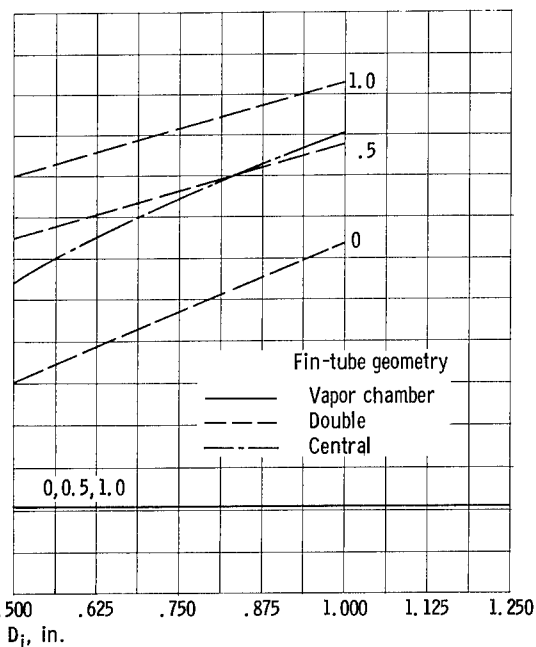


Figure 22. - Number of radiator tubes comparison at peak heat rejection per unit weight for vapor-chamber, double, and central fin-tube radiators. Radiator inlet temperature, 1700°R ; fin segment planform area, 10 square inches; $h_B = h_C = 10^4$ Btu per hour per square foot per $^{\circ}\text{F}$.

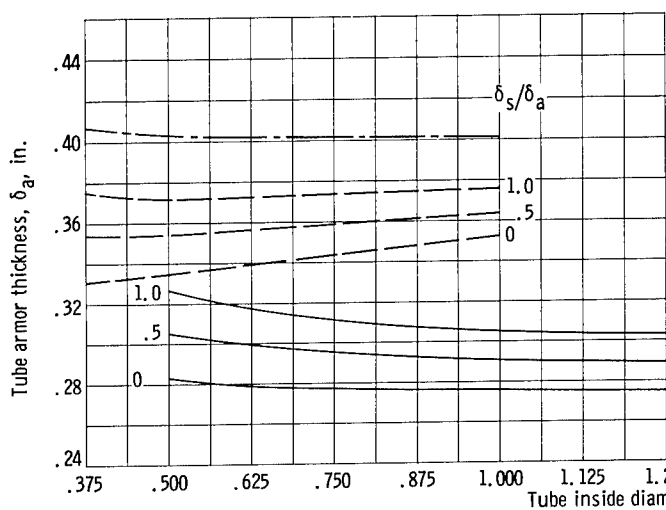


(a) Electrical power output, 500 kilowatts; columbium fins and tube armor; capillary weight, 0.2 pound mass per square foot.

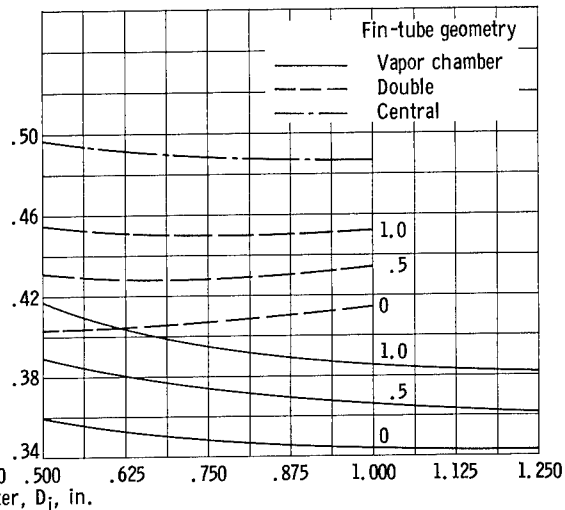


(b) Electrical power output, 1 megawatt; beryllium fins and tube armor; capillary weight, 0.1 pound mass per square foot.

Figure 23. - Comparison of fin thickness at peak heat rejection per unit weight for vapor-chamber, double, and central fin-tube radiators. Radiator inlet temperature, 1700°R ; fin segment planform area, 10 square inches; $h_B = h_C = 10^4$ Btu per hour per square foot per $^{\circ}\text{F}$.

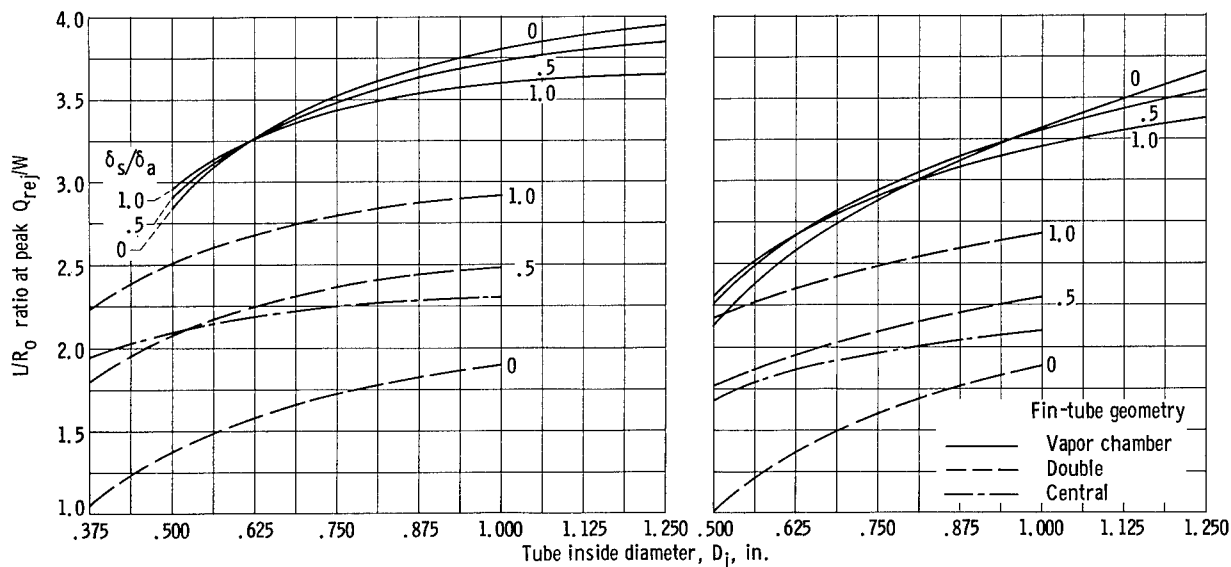


(a) Electrical power output, 500 kilowatts; columbium fins and tube armor; capillary weight, 0.2 pound mass per square foot.



(b) Electrical power output, 1 megawatt; beryllium fins and tube armor; capillary weight, 0.1 pound mass per square foot.

Figure 24. - Comparison of tube armor thickness at peak heat rejection per unit weight for vapor-chamber, double, and central fin-tube radiators. Radiator inlet temperature, 1700°R ; fin segment planform area, 10 square inches; $h_B = h_C = 10^4$ Btu per hour per square foot per $^{\circ}\text{F}$.



(a) Electrical power output, 500 kilowatts; columbium fins and tube armor; capillary weight, 0.2 pound mass per square foot.

(b) Electrical power output, 1 megawatt; beryllium fins and tube armor; capillary weight, 0.1 pound mass per square foot.

Figure 25. - Comparison of radiator L/R_0 ratio at peak heat rejection per unit weight for vapor-chamber, double, and central fin-tube geometries. Radiator inlet temperature, 1700°R ; fin segment planform area, 10 square inches; $h_B = h_C = 10^4$ Btu per hour per square foot per $^\circ\text{F}$.

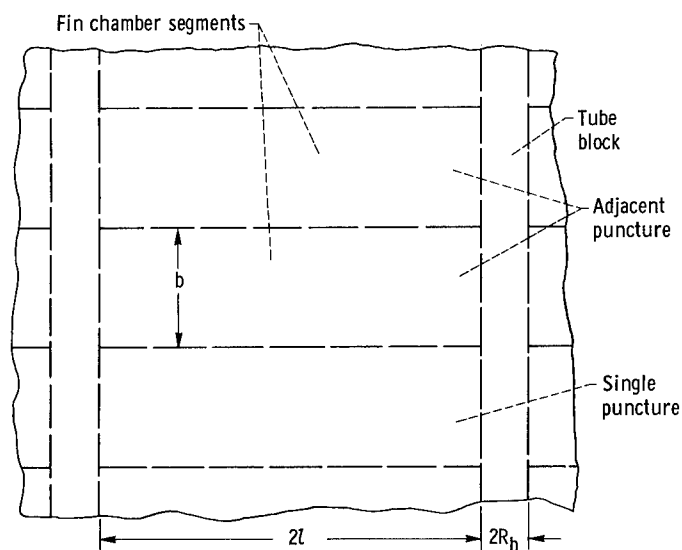


Figure 26. - Vapor-chamber segmented fin puncture arrangement.

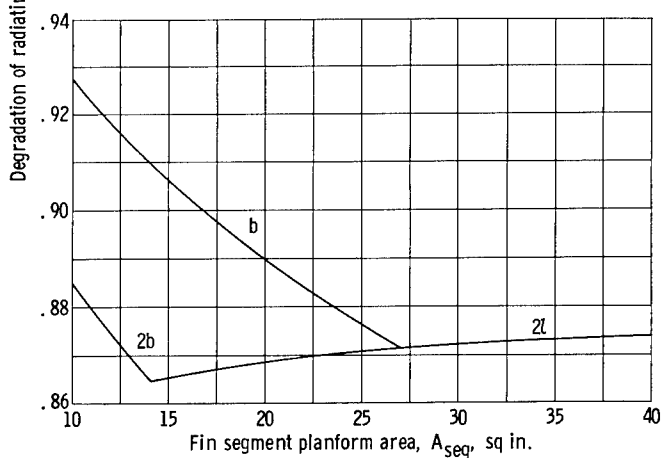
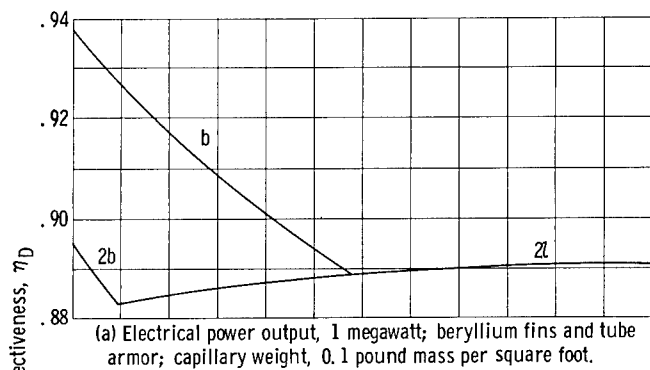
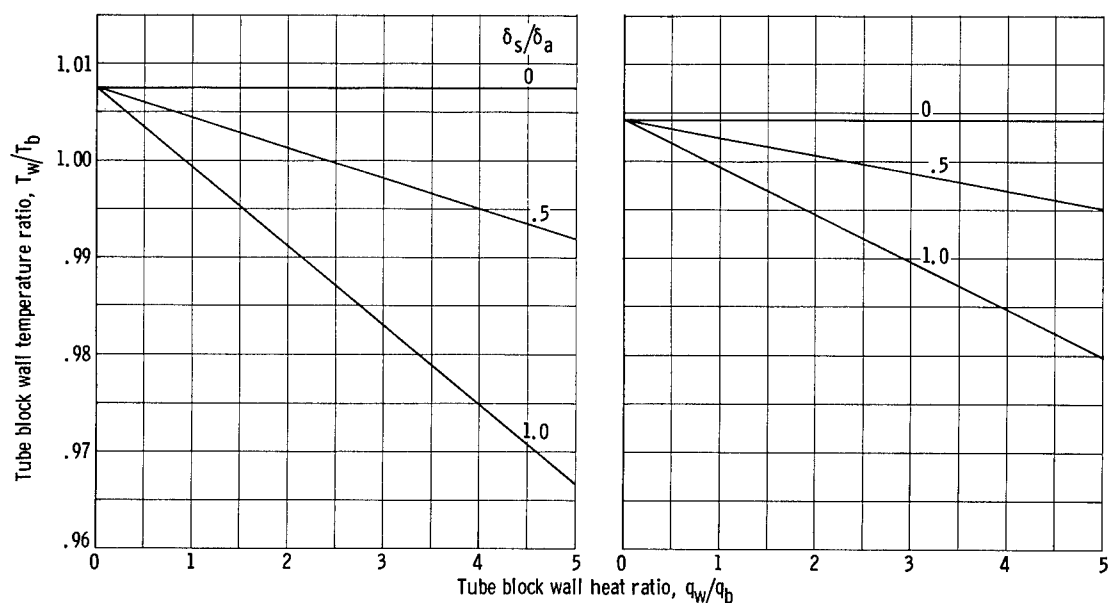


Figure 27. - One-dimensional radiator thermal degradation with fin planform area for vapor-chamber fin-tube geometry. Tube inside diameter, 0.75 inch; $h_B = h_C = 10^4$ Btu per hour per square foot per $^{\circ}F$; $\delta_S/\delta_a = 0.5$; $N_S/N = 0.75$.



(a) Electrical power output, 500 kilowatts; columbium fins and tube armor; inside tube diameter, 0.50 inch; static fluid temperature at tube inlet, 1623°R ; tube armor protection thickness, 0.0276 foot.

(b) Electrical power output, 1 megawatt; beryllium fins and tube armor; inside tube diameter, 0.75 inch; static fluid temperature at tube inlet, 1630°R ; tube armor protection thickness, 0.03152 foot.

Figure 28. - Ratio of tube block side wall to outer wall temperature for vapor-chamber fin-tube geometry. Radiator inlet temperature, 1700°R .

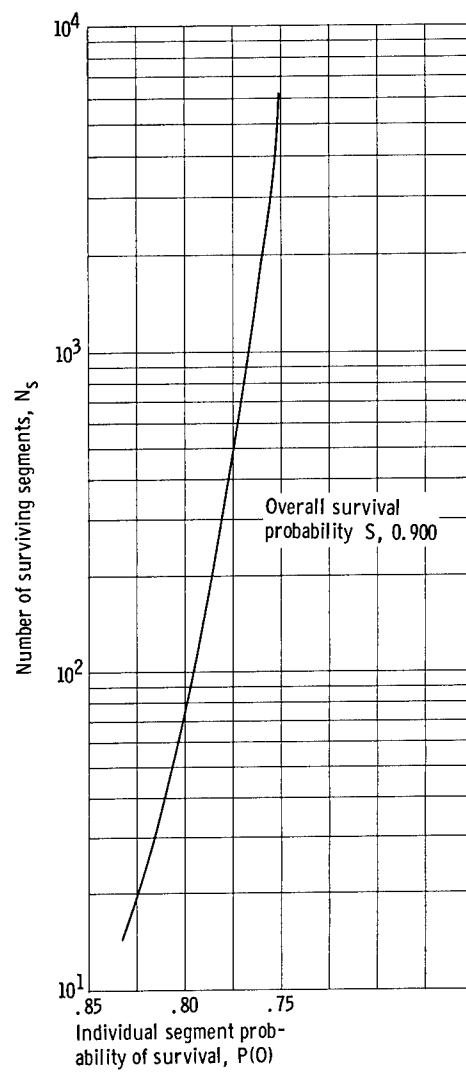


Figure 29. - Nonpenetration probability of one segment of segmented fin for $N_s/N = 0.75$.